AFOSR-TR- 85-0080

A FUNDAMENTAL STUDY OF LIQUID PHASE PARTICLE BREAKUP

FINAL REPORT

Revised December 1984

Approved for public release;
distribution unlimited.

SDL
SPECTRON DEVELOPMENT LABORATORIES, INC.

AFOSR-TR- 85-0080

A FUNDAMENTAL STUDY OF LIQUID PHASE PARTICLE BREAKUP

FINAL REPORT

Revised December 1984

Approved for public release;
distribution unlimited.

SDL No. 84-2193-11F

Prepared for:

Dr. Leonard Caveny/NA
Director, Aerospace Sciences
AIR FORCE OFFICE OF SCIENTIFIC RESEARCH
Building 410
Bolling Air Force Base, D.C. 20332

Under Contract No.
F49620-81-C-0032

SDL
SPECTRON DEVELOPMENT LABORATORIES, INC.
3303 HARBOR BLVD., SUITE G-3, COSTA MESA, CA 92626 • (714) 548-8477

Approved for public release;
distribution unlimited.

TABLE OF CONTENTS

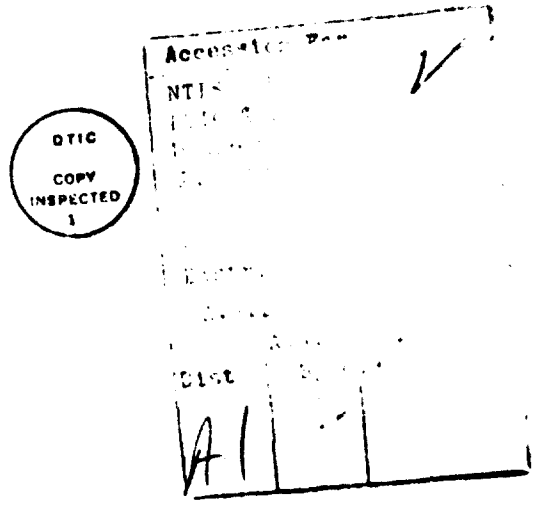

LIST OF FIGURES

1.0 INTRODUCTION

Combustion efficiency of aluminized propellants in solid rocket motors is reduced by incomplete aluminum combustion and two-phase nozzle flow losses. The combustion of aluminized propellants can produce large Al/Al_2O_3 agglomerates. The agglomerate dynamics within the combustion chamber and nozzle have a significant influence on the overall combustion efficiency of the motor[1-5]. Agglomerates are subjected to large aerodynamic loads within the rocket nozzle where the gas phase experiences a more rapid acceleration than the agglomerates. The drag load deforms the agglomerates and if of sufficient magnitude result in breakup. The smaller fragments have faster velocity and thermal equilibrium times and have higher combustion rates. For maximum combustion efficiency the aluminum fragments must completely oxidize, and achieve kinetic and thermal equilibrium with the gas phase. As a direct result of agglomerate breakup, the aluminum combustion rate is increased, and the thermal energy released is more efficiently transferred into exhaust kinetic energy.

Photographic observations obtained in windowed rocket motors[6-7] and combustion bombs[8-10] indicate relatively large agglomerates (100μm - 500μm) are formed on the propellant surface and entrained in the combustion flow; however, particle size measurements obtained from sampling the exhaust plumes[11-15] indicate small mean particle diameters (<10μm). These small exhaust plume particles apparently result from the breakup of the larger agglomerates during the nozzle expansion

process. Observations of agglomerate breakup in a laboratory scale rocket nozzle revealed an adequate correlation with Weber number; however, neither the physical process of breakup nor the fragment size distribution was resolved[16].

The objective of this research is to obtain physical data to characterize the mechanisms of aerodynamic droplet breakup. Experiments have been completed in which conventional liquids (water, alcohol and glycerine/water mixtures) and a liquid metal (mercury) was studied. The primary goal of the conventional liquid experiments was to examine the effect of liquid properties (viscosity and surface tension) on the breakup mechanism, time scale, and fragment size distribution. The goal of the liquid metal experiments was to examine the effect of the much higher surface tension more characteristic of liquid aluminum.

A key element of the experimental effort is the use of nonintrusive laser diagnostics including pulsed laser holography and laser Doppler velocimetry (LDV). The exceptional temporal and spatial resolution of pulsed laser holography provided the ability to resolve the mechanism of breakup and the size distribution of the fragments. Laser Doppler velocimetry was used to determine drop velocity distributions along the nozzle revealing the rapid acceleration of the flattened droplets and then, surprisingly, the milder acceleration of the fragments. The high drag to mass ratio of the flattened droplets was expected and resolved during the initial phase of the breakup process.

2.0 EXPERIMENT CONSIDERATIONS

Aerodynamic droplet breakup is characterized by the magnitude and duration of the aerodynamic forces. For nozzle contractions, the droplets are loaded as a result of the higher gas phase acceleration. The droplets respond to the aerodynamic forces by deforming and accelerating. The initial acceleration scales with the initial diameter; however, as the pressure forces flatten the droplet, increasing its cross-sectional area, the drag load and the acceleration increases rapidly. This sequence of events can, of course, lead to catastrophic deformation and droplet breakup if the slip velocity is of sufficient magnitude and duration.

The liquid surface tension is used to scale the aerodynamic load forming the Weber number:

$$We = \frac{\rho \, \Delta v^2 \, \phi_d}{\sigma_d} \qquad (1)$$

ρ = density
Δv = slip velocity
ϕ = diameter
σ = surface tension

The duration of the aerodynamic loading can be scaled by the natural period for hydrodynamic oscillation, which is a measure of the droplet response time:

$$\tau_n \simeq \frac{\rho_d \phi_d^3}{\sigma_d}^{1/2} \tag{2}$$

For nozzle accelerations, an additional time scale exists; namely the time required for velocity equilibrium, τ_v. Assuming the droplet Reynolds number relative to the gas phase is sufficiently high (i.e., $Re > 10^3$), the drag coefficient for rigid droplets is approximately unity and the corresponding time scale is

$$\tau_v = \frac{\rho_d \phi_d}{\rho \Delta v} \tag{3}$$

However, since the liquid droplets are not rigid, the droplet cross section and the associated drag load increase rapidly within the nozzle contraction. Therefore, the time scale for liquid droplet velocity equilibrium is no doubt faster than the rigid droplet estimate.

A few liquid types were selected to examine the effect of liquid properties such as surface tension and viscosity. For the conventional liquids, water and alcohol were selected for the surface tension series;

and water and a glycerine water (57/43) mixture were selected for the viscosity series. The mixture was selected to achieve a viscosity ten times that of water.

A second series of experiments were designed to examine the breakup dynamics of high surface tension liquid metals. Mercury was selected because of its compatibility with the droplet generation technique and with room temperature air flow.

2.1 Nozzle Facility

An experiment was designed in which droplet breakup could be investigated in a nozzle contraction. The nozzle was designed to allow droplet injection upstream of the contraction. Windows formed the sides of the two-dimensional nozzle allowing observation of the droplet interaction. The gas was delivered from a settling chamber through a sintered metal throttle to the nozzle plenum where the droplets were injected. The nozzle area ratio was eight, Figure 1. For the conventional liquid experiments, the nozzle was operated at subsonic exit velocities. However, for the liquid metal experiments, higher dynamic pressures were required to achieve droplet breakup. Higher droplet loading was achieved by increasing the gas velocity and hence the slip velocity. In fact, the nozzle exhaust was modified to allow sonic flow in the nozzle throat for the liquid metal experiments, although droplet breakup occurred upstream of the throat.

Piezoelectric droplet generators were constructed to produce highly monodisperse droplet streams. The basic design was that of modern ink-jet printers. The complete droplet generator is composed of

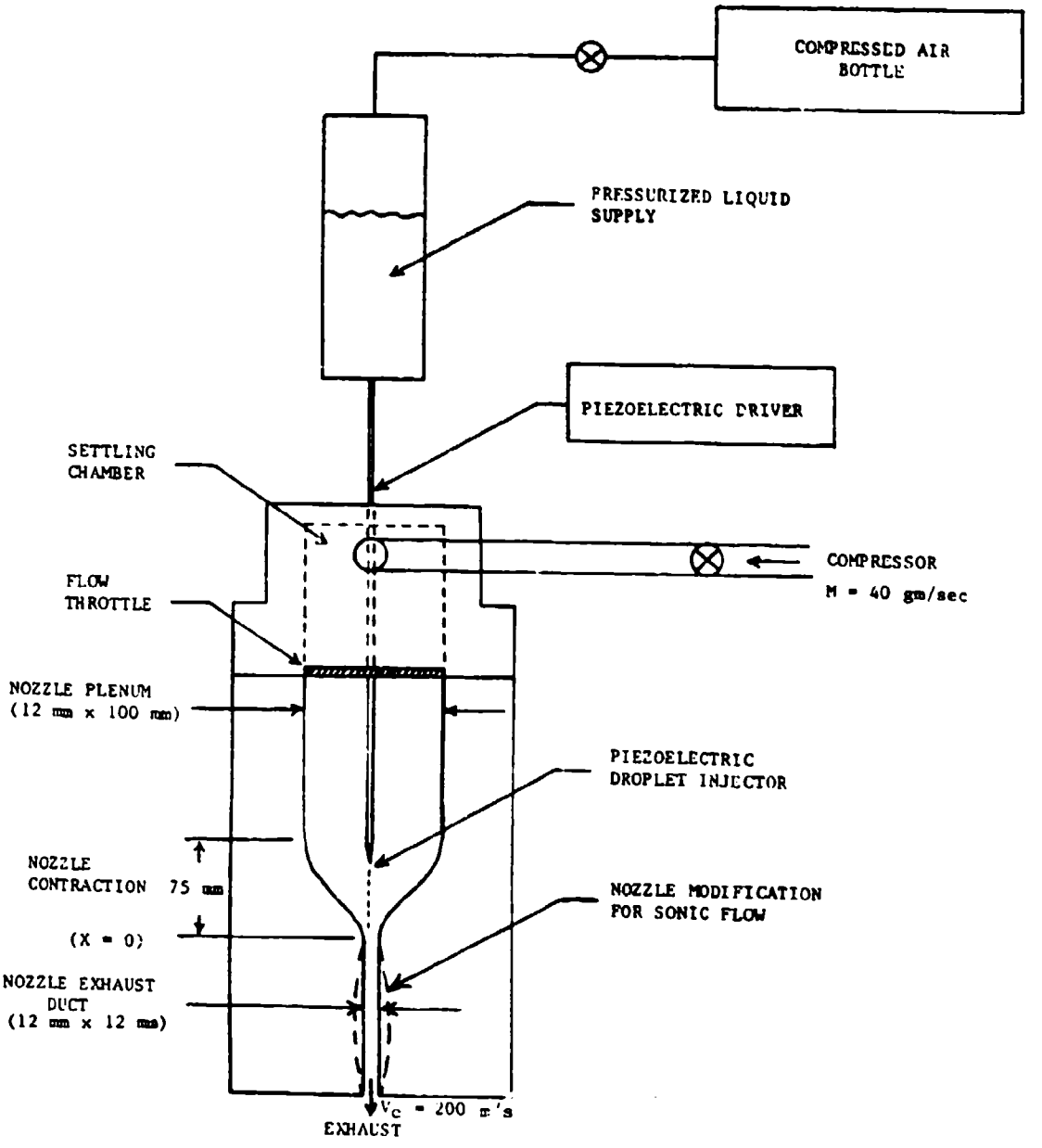

Figure 1. Nozzle Facility with Piezoelectric Droplet Injector

a liquid supply tank, an electrical driver, and the ink-jet devices (Figure 1). The size of the droplets generated by our devices was variable from about 1.5 to 3.0 times the orifice diameter by decreasing the excitation frequency. For conventional liquids, droplets were generated from 160 μm to 400 μm in diameter, and for mercury, droplets were generated from 190 μm to 560 μm. The droplet generator operating conditions are listed in Table I for the conventional liquids and mercury.

TABLE I. DROPLET GENERATOR OPERATING CONDITIONS

LIQUID	DIAMETER		EXCITATION FREQUENCY (kHz)
	TIP (μm)	DROPLET (μm)	
Water	100 120 190	160 220 410	10.6 8.0 0.8
Alcohol	100 150	164 265	11.2 9.0
Glycerine/ Water	120	240	7.2
Mercury	130 130 190	190 300 560	10.0 1.5 0.8

2.2 Droplet Holography

Holographic observations of the droplet interaction within the nozzle contraction were produced. The holocamera imaging optics were configured with object-to-hologram image magnifications of one and five (Figure 2). The large field-of-view optics (ϕ = 100 mm diameter, 1x magnification) were used in the initial experiments in which the droplet velocities were measured along the nozzle. Double exposure (Δt=10μs) holography is used to observe droplet velocity. Smaller field-of-view optics (ϕ = 25 mm diameter, 5x magnification) were used to record high resolution observations of the droplet breakup process. For this case, external triggering was required to center the droplet position in the hologram. With premagnification (5x) the holocamera spatially resolves 4μm in reconstruction. Since the holograms are recorded in 10^{-8} seconds, droplets of order 10μm diameter can be resolved at velocities approaching 10^3 m/s. For these experiments the droplet velocities were limited to about 100 m/s.

2.3 Laser Velocimeter

Droplet and gas phase velocities were obtained using laser Doppler velocimetry (LDV), Figure 3. This technique is based on laser light scatter by droplets or seed particles in the flow. A single laser beam (Spectra Physics, Model 124, 15 m watt) is split into two equal intensity beams which intersect at the desired measurement point in the flow. Electromagnetic interference between the two laser beams occurs at the intersection region resulting in fringe formation. The fringes are parallel planes of high intensity (constructive interference)

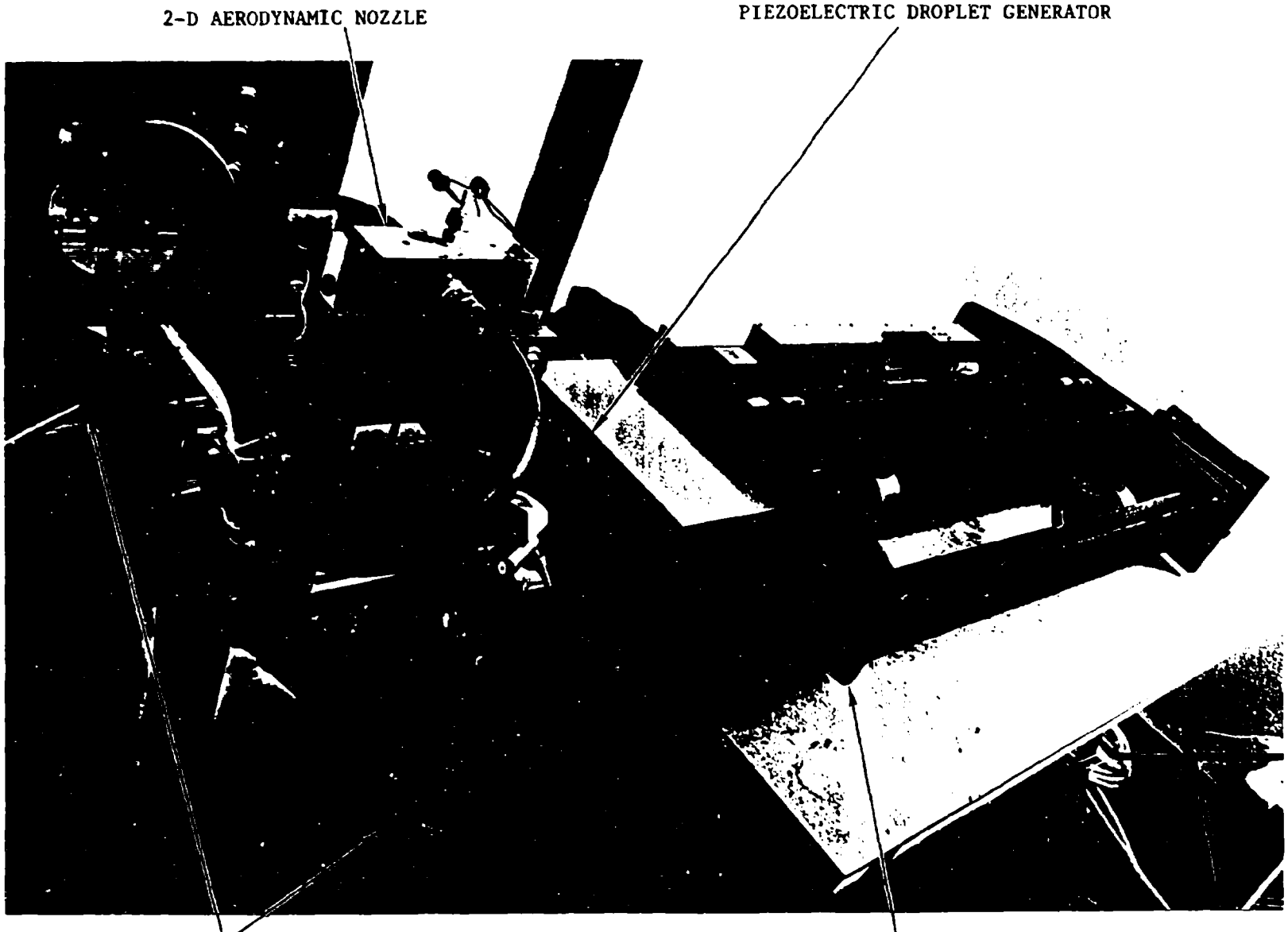

Figure 2. Aerodynamic Droplet Breakup Experiment

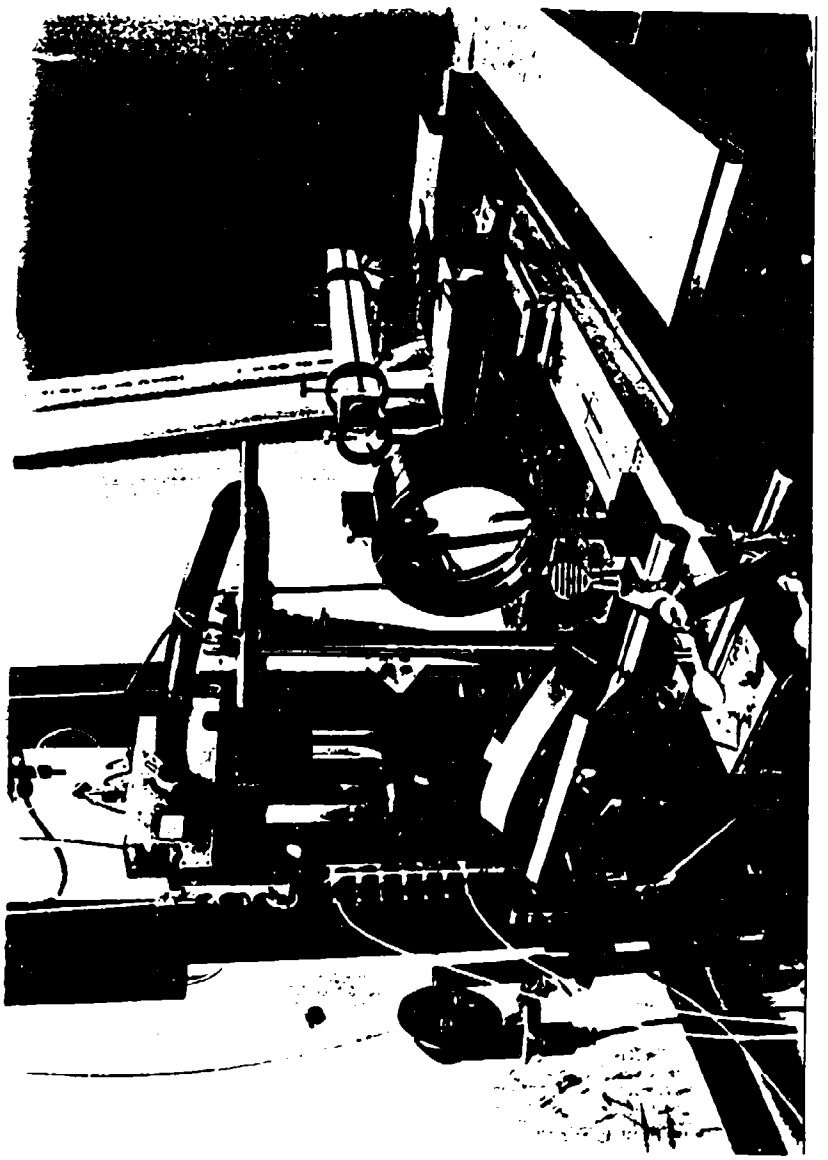

Figure 3. Laser Doppler Velocimeter Installation

alternating with lower intensity (destructive interference). For these experiments the spacing between successive fringes was 7μm. Light scattered by particles in the flow produces signals modulated by the fringe pattern intensity. The electronic signal processor (Macrodyne, 2000 Series, LDV Processor) measures the time between successive fringes from which particle velocity is obtained. Distributions of a large number of events (typically 10^4) were obtained at each measurement point in the flow from which mean velocities were obtained. The droplet and fragment velocity distributions were measured with the laser velocimeter. The mean velocity is calculated at each station. The droplet velocity profile was integrated to determine the elapsed time and differentiated to determine the acceleration. The gas/droplet slip velocity was used to determine the Weber number (based on initial droplet diameter) history along the nozzle. Hence, both the Weber number at droplet breakup and the breakup time were determined.

3.0 CONVENTIONAL LIQUID EXPERIMENTS

A series of experiments was conducted to observe the droplet deformation and fragmentation processes with holography and to determine the droplet and fragment dynamics with laser velocimetry. The experiments were conducted with three liquid types. For each liquid with a corresponding surface tension, a parametric set of trajectory calculations were performed for various nozzle exit velocities, and droplet sizes. In an early series of experiments, the rigid droplet trajectory estimates were found to grossly over estimate the Weber number history when compared to experiment data. In the experiments, the liquid droplets were found to achieve much higher accelerations just prior to breakup. The mechanism for enhanced acceleration was presumed to be droplet flattening, and as a result the droplet Weber numbers were lower than predicted. The gas velocity was increased so that breakup occurred. The test conditions are listed in Table II; including the liquid type, droplet size, maximum gas velocity, the slip velocity and Weber number at breakup, the breakup time, and the period of the first natural frequency (i.e. Eqn. 2). The breakup times were measured relative to the time at which the Weber number exceeded five.

3.1 Results

The holographic investigation revealed that the breakup mode for nozzle accelerations was similar to the breakup modes observed for shock wave accelerations. Initially the droplet flattens under the high

TABLE II. TEST MATRIX

SERIES	LIQUID	DROPLET (μm)	GAS VELOCITY (m/s)	SLIP VELOCITY (m/s)	WEBER NUMBER	BREAKUP TIME (ms)	NATURAL PERIOD (ms)
1	Water	140	100	82	17	2.25	0.20
2		160	190	135	53	0.9	0.25
3		410	100	78	49	2.2	1.0
4		410	190	84	56	1.7	1.0
5	Alcohol	165	100	77	58	1.3	0.40
6		176	190	105	110	1.6	0.44
7		265	160	80	93	1.5	0.82
8	Glycerine, 57% Water, 43%	240	170	88	33	0.93	0.44
9	Mercury	190	310	165	17	0.77	0.45
10		300	310	135	16	0.80	0.89
11		560	310	119	22	2.8	2.3

pressure exerted on the stagnation point (Figure 4). As the droplet flattens, its radius of curvature increases and the stagnation pressure is felt over a larger area. The center of the droplet is eventually pushed downstream of the outer edge forming a thin membrane in the shape of a bag (Figure 5). When the bag bursts, very small fragments are formed; however, considerable mass still remains in the annular ring. The annular ring fails later producing the larger fragments as has been reported by others[17].

A glycerine/water mixture was used to investigate viscous effects. The mixture was selected to obtain a viscosity 10 times that of water ($\gamma_{mixture}$ = 10 cp). The significant effect of viscosity is to modify the rate of deformation in the streamwise and radial directions. Specifically, the rate of expansion in the streamwise and radial directions are observed to be about equal; and as a result, the droplets expand radially to about 7 times the original diameter (Figure 6). For the lower viscosity case, radial expansion is limited to about a factor of four or five. The mechanism of droplet breakup is not significantly altered; however, some details are strikingly affected. For the higher viscosity case, geometric symmetry is maintained throughout substantial portions of breakup event; whereas for the lower viscosity case, the deformation quickly becomes asymmetric or random.

The laser velocimeter was used to obtain velocity distributions (Figure 7). Initially the velocity distribution is narrow; however, the distribution broadens substantially within the breakup region. Finally, as a result of the large increase in the mean velocity of the fragments

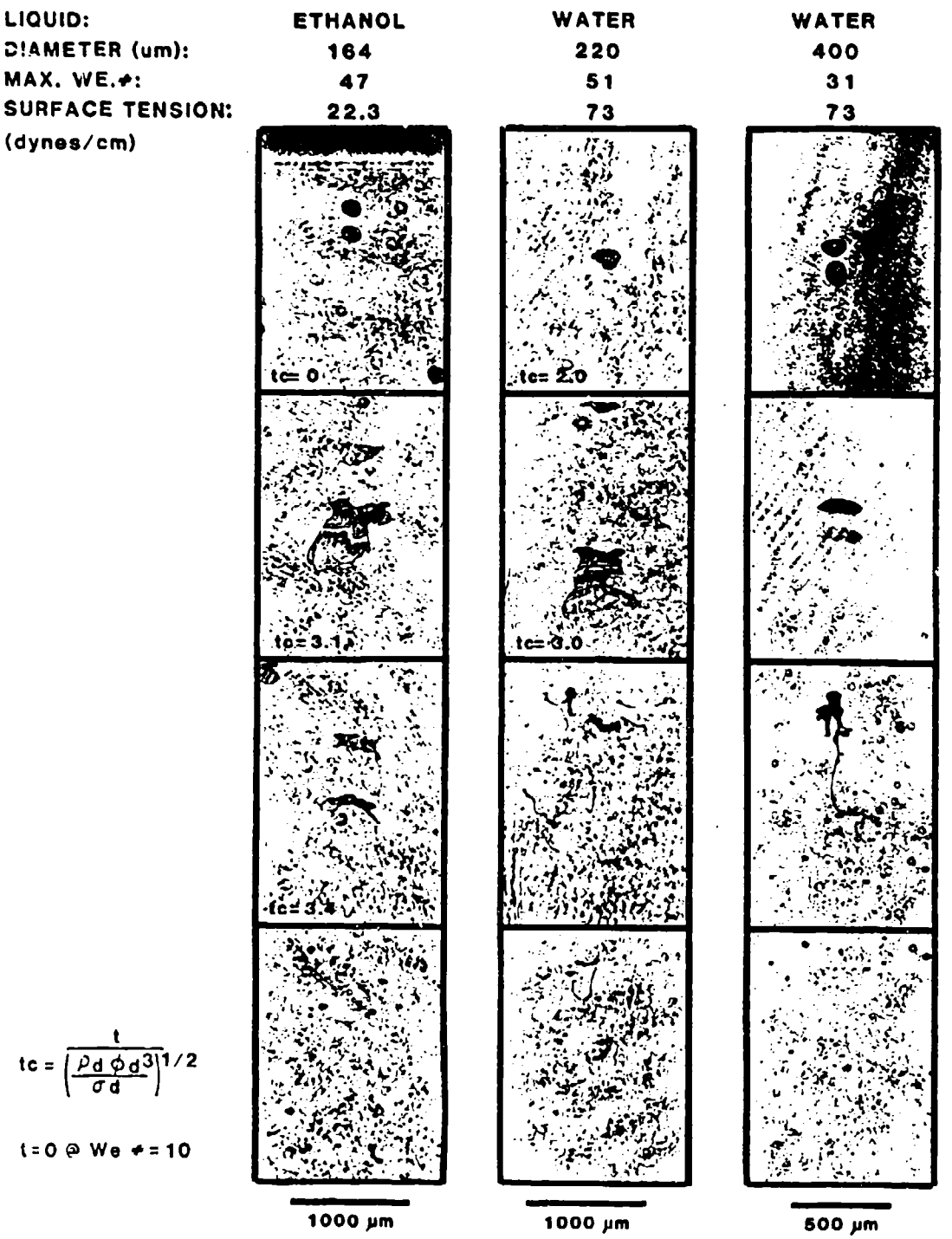

Figure 4. Surface Tension Effects on Droplet Breakup

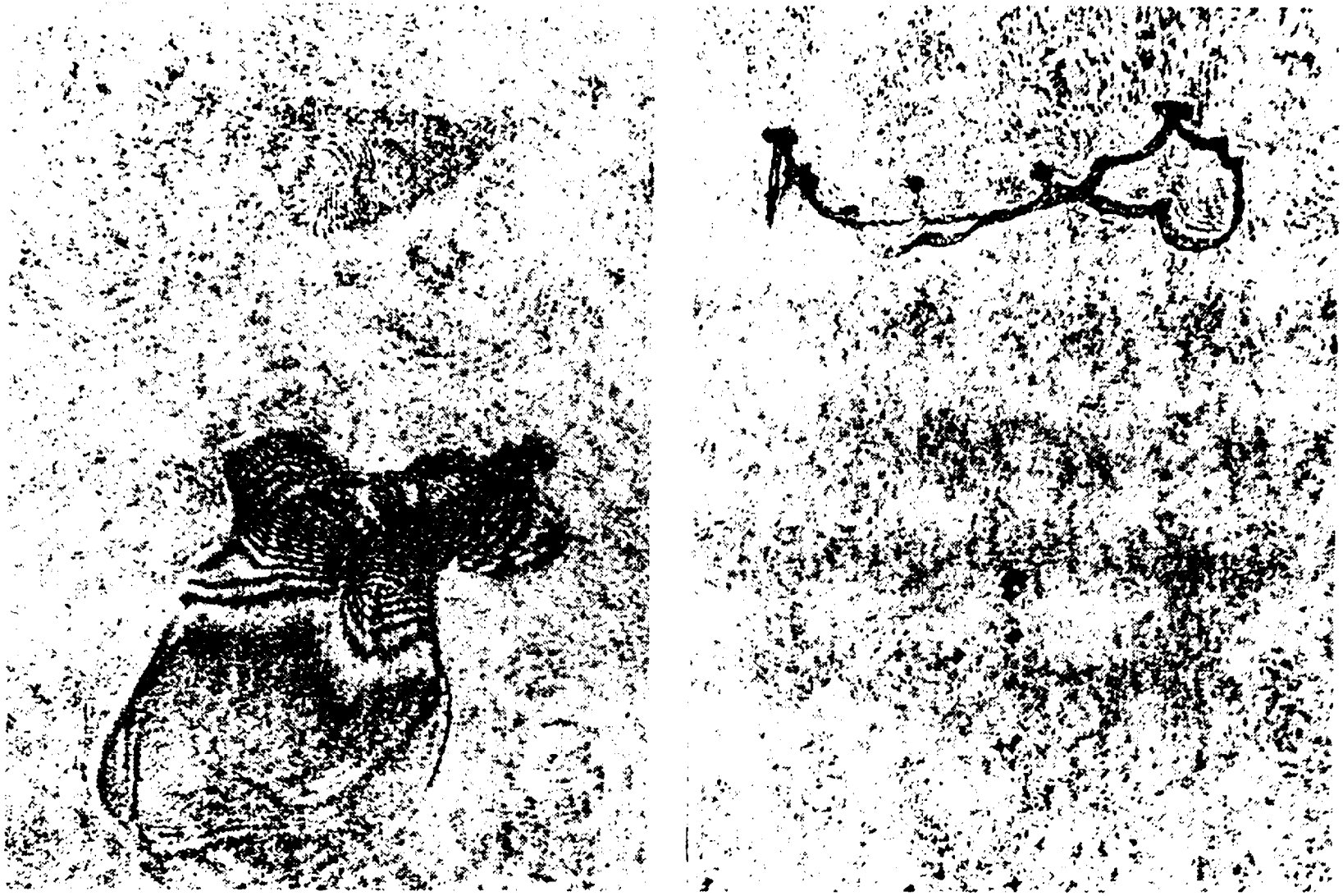

Figure 5. Holography Data, Alcohol Droplets (Series 5, Table II)
(a) Double Pulse (ΔT = 25 μs) Bag Breakup Mode
(b) Ring Structure Observed Later in Breakup Event

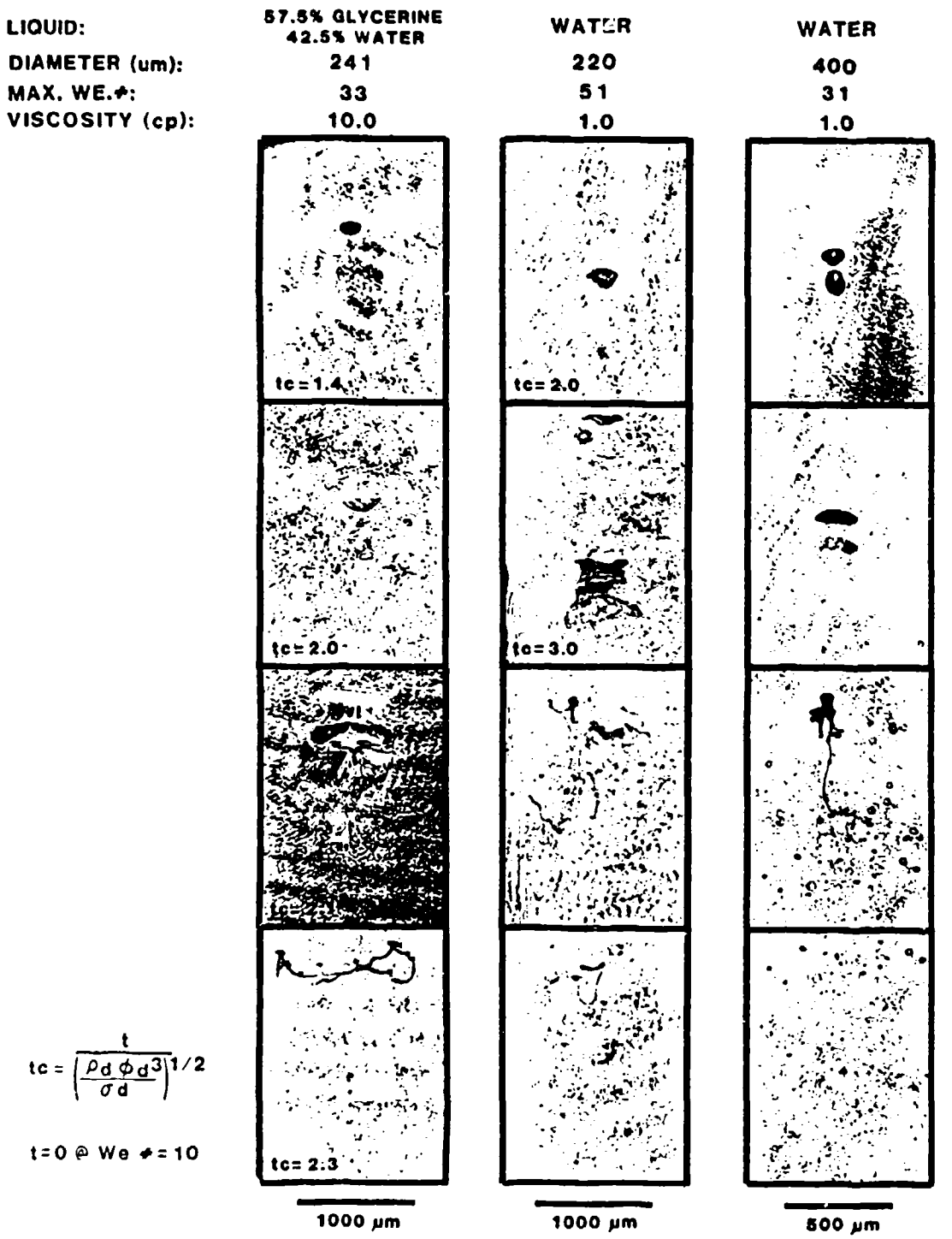

Figure 6. Viscosity Effects on Droplet Breakup

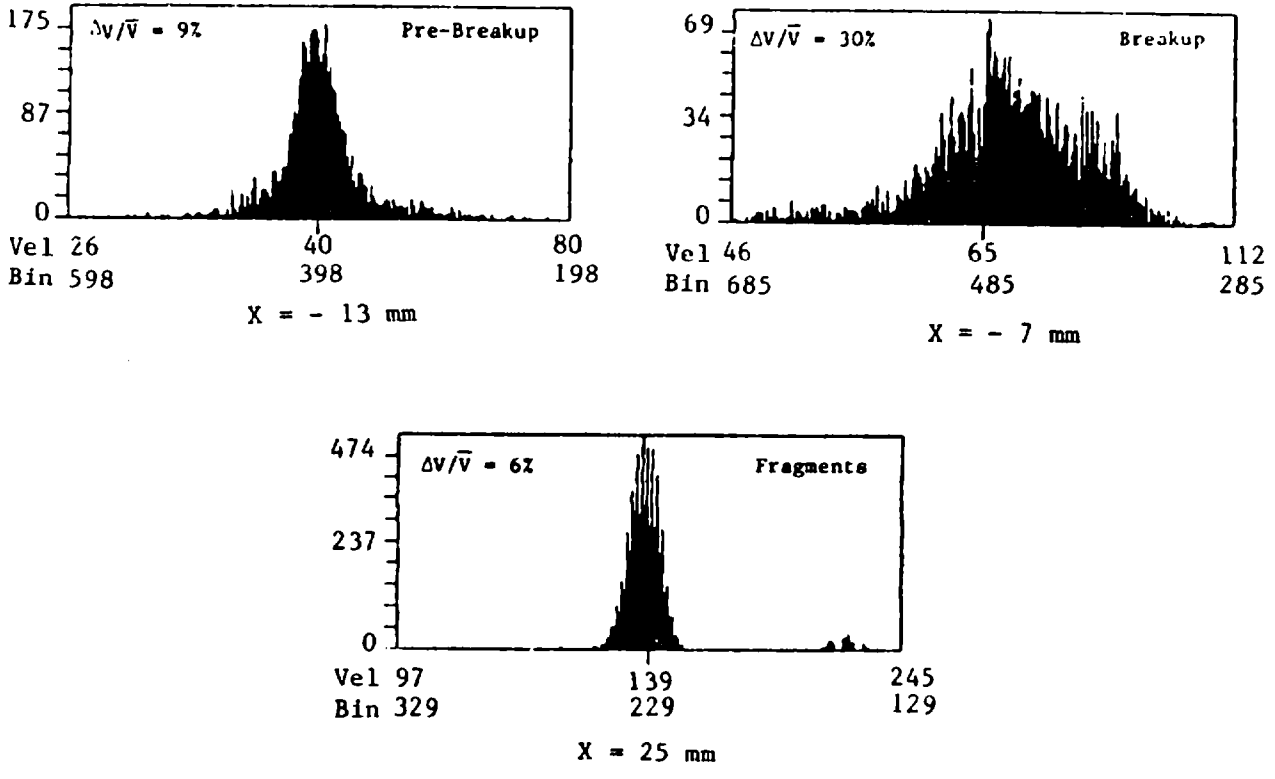

Figure 7. Laser Doppler Velocimetry Data, Point Velocity Distributions Along Nozzle (See Figure 1 for Nozzle Coordinates)

the relative width of the distribution is reduced. The broad distribution within the breakup region should not be confused with turbulence, but should be associated with the breakup phenomena. Fairly mild accelerations were observed until the droplet begins to deform and flatten. The drag to mass ratio of the flattened droplet is considerably higher than for the spherical geometry; and as a result the droplet experiences extreme accelerations just before breakup. This final acceleration, of course, reduces the peak slip velocity and Weber number and must be accurately modeled if the Weber number at breakup is to be predicted.

The Weber number profiles for water droplets are shown in Figure 8. The position at which breakup occurs moves downstream if the droplet size or the nozzle velocity is reduced. As a result of reduced size or velocity the peak Weber number is reduced; and eventually, a condition is reached for which droplet breakup does not occur within the nozzle contraction. In our experiments with water droplets, this condition was reached only for the smallest droplet size, 150 μm, and the smallest velocity rise, 100 m/s, in which case, the Weber number did not exceed 20 and failure did not occur in the nozzle contraction. Thus, for a given velocity rise in the nozzle contraction, there exists a boundary in the Weber number/position plane at which droplet breakup occurs.

Since the breakup position is dependent on the nozzle velocity rise, consider instead the time history of loading. This is a more unified approach since it is the loading duration which produces droplet deformations and eventually breakup. A zero time must be selected and

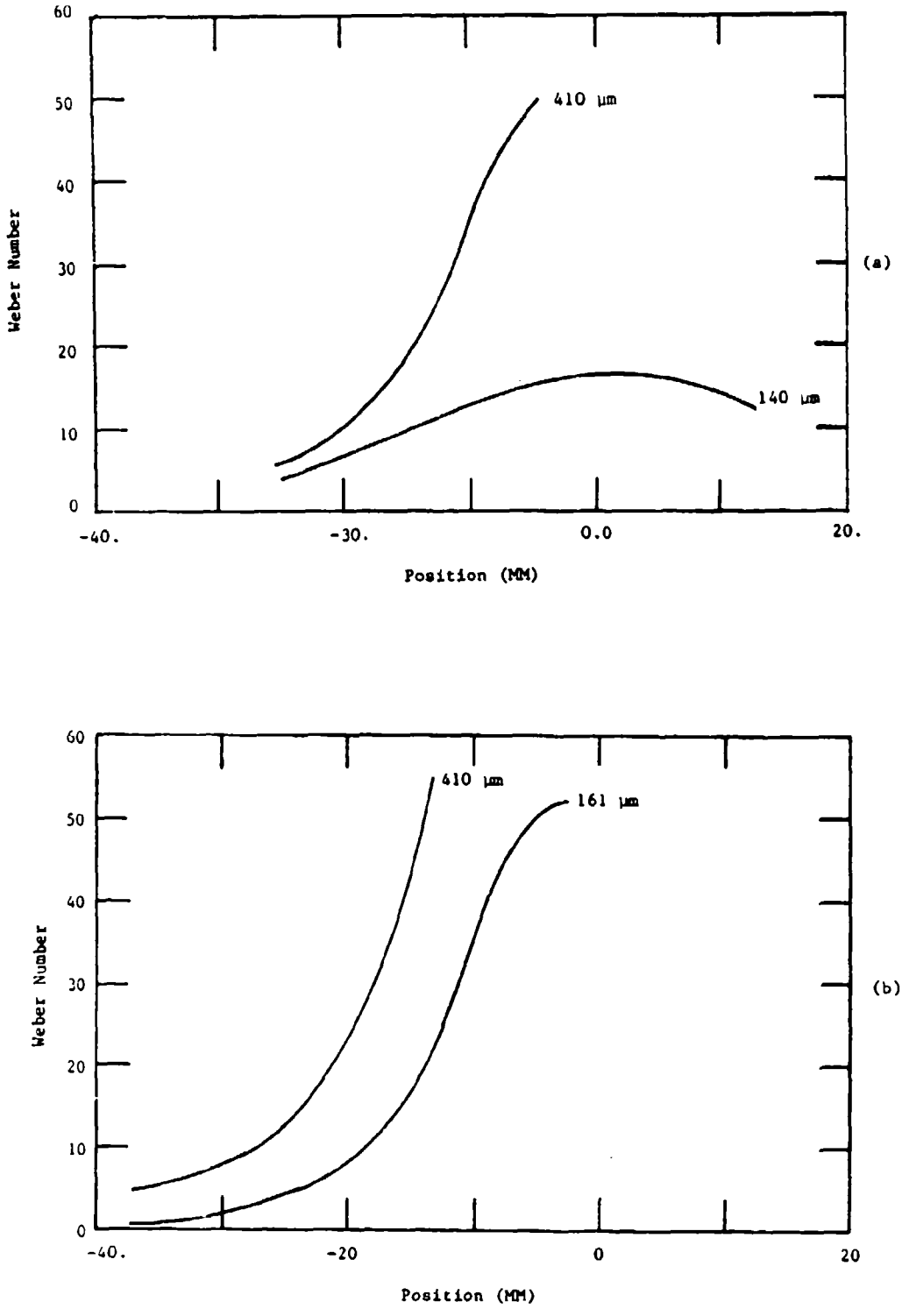

Figure 8. Water Droplet Weber Number Profiles
[Nozzle Velocity Rise: (a) 100 m/s and (b) 190 m/s]

we have chosen the time at which the Weber number reaches five. The Weber number (loading) is plotted against relative time and different velocity rise and droplet size conditions compared. The relative time has been normalized by the period of the first natural frequency (Eqn. 2).

The water droplet data (Figure 9) fall along a boundary starting at a Weber number of about 50 and time of one and extending to very low Weber numbers at long times. One of the alcohol data points is near the water boundary, while the others are at much higher Weber numbers (i.e., over 100). The glycerine droplet data point indicates that breakup occurred at a lower Weber number than for water droplets. Holographic observations revealed that the glycerine droplets flattened to a much larger cross section as a result of the increased viscosity. The additional cross section increased the drag and acceleration resulting in a lower Weber number trajectory. The fundamental result is that gradual loadings produced by nozzle accelerations allows the droplets to reach higher Weber numbers than are critical for impulsive loading as produced in shock tube simulations.

3.2 Breakup Parameters

Weber number effect on breakup was studied by changing both droplet size and nozzle velocity. The bag was still observed to expand downstream of the ring; however, after the bag bursts, the ring exhibits more random distortion with increasing Weber number (Figure 10). Increased Weber number was observed to decrease the fragment size. The

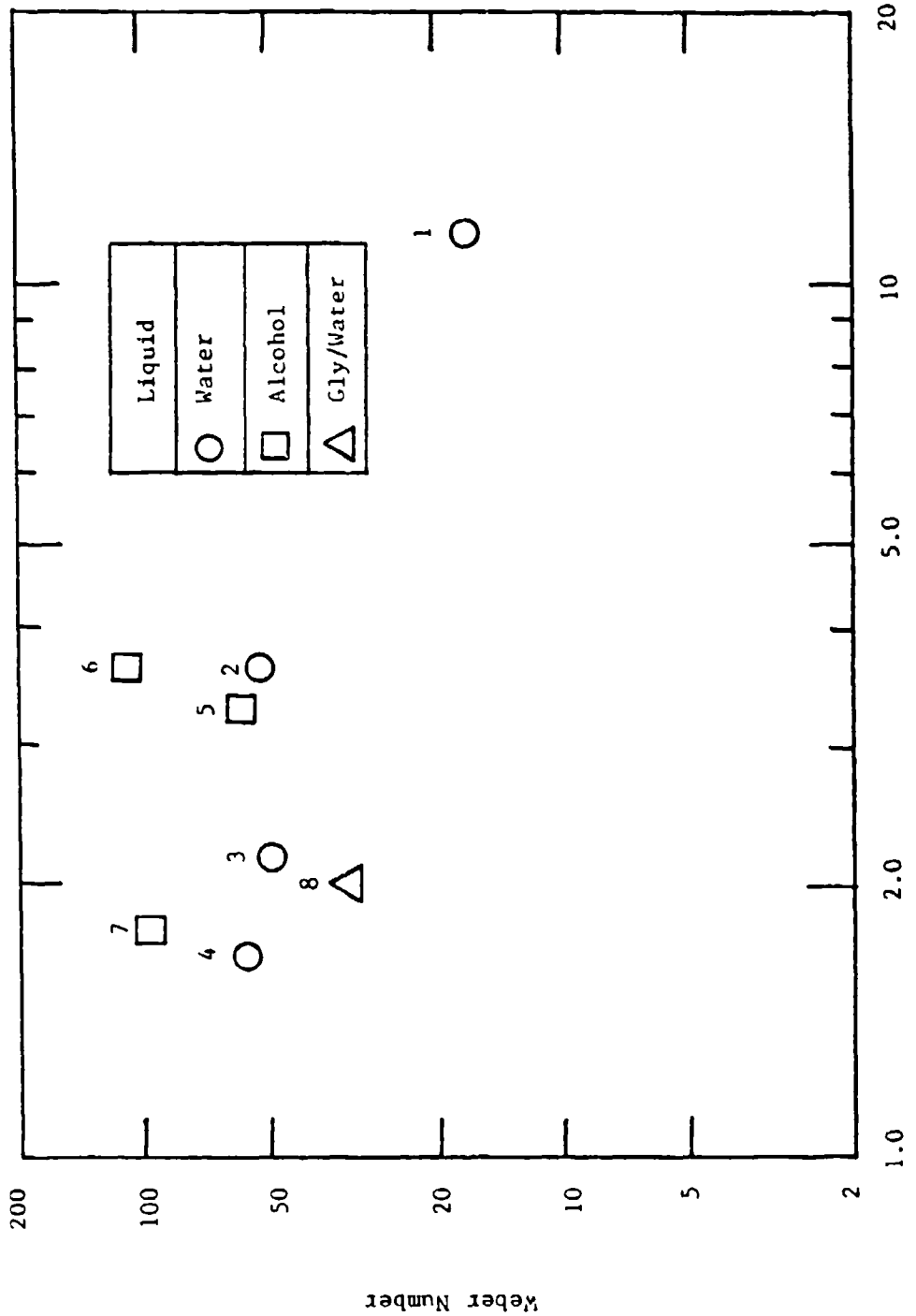

Figure 9. Critical Weber Numbers and Associated Time Durations of the Breakup Event: Series Number (i.e. 1-8) refers to Table II

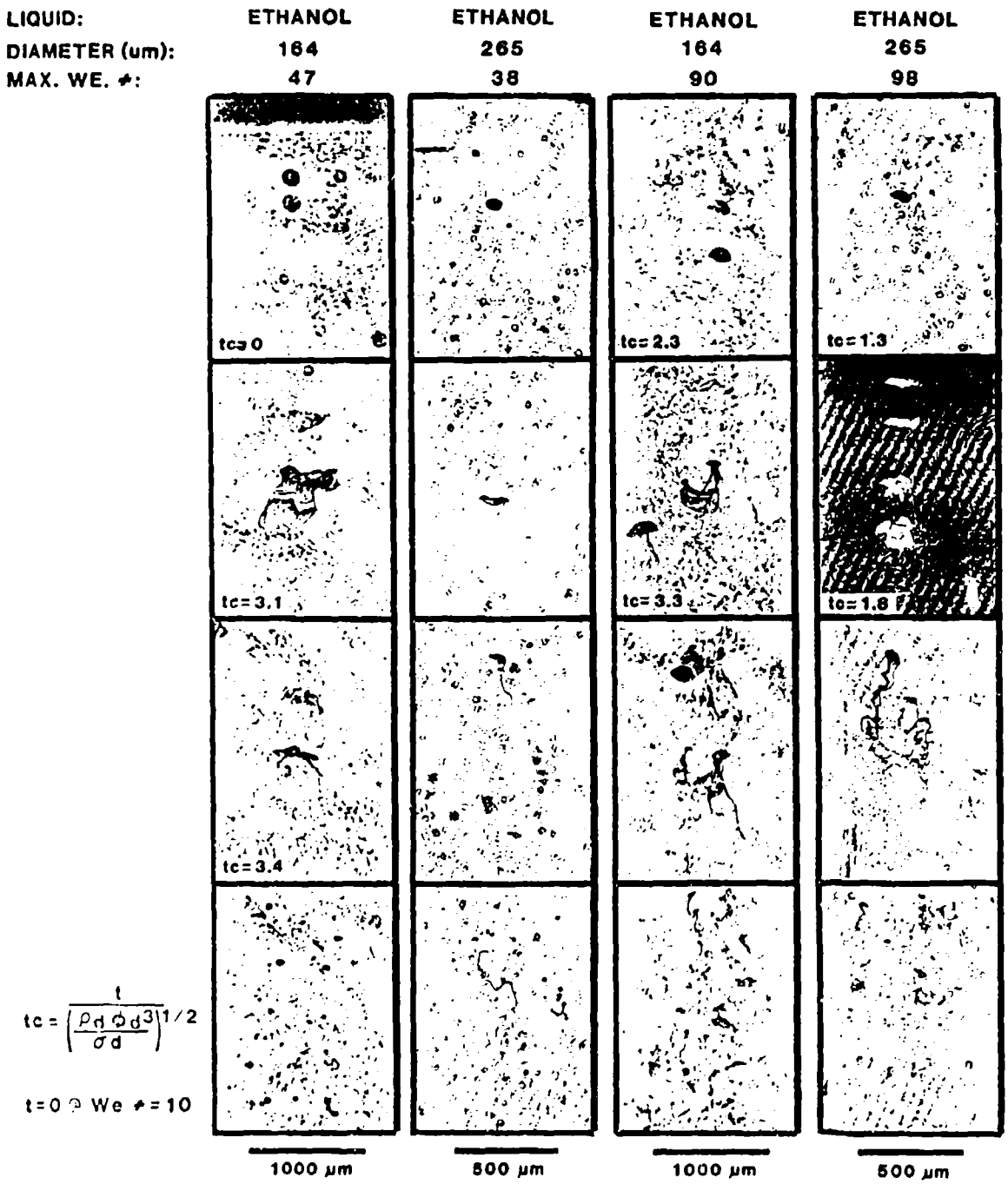

Figure 10. Weber Number Effects on Ethanol Droplet Breakup

mean fragment size is plotted against peak Weber number (Figure 11). The mean fragment size based on acceleration (Equation 4) is also plotted. The mean fragment size was estimated by using a force balance on the fragments. The drag load was written in terms of the slip velocity, fragment size, and a drag coefficient based on the Reynolds number. The mass was written in terms of the fragment size and density (the fragments are assumed spherical, a fact confirmed by holographic data); and the acceleration was measured.

The force balance resulted in an equation for the fragment size, ϕ, as follows:

$$F = MA$$

or

$$q\ C_D\ \frac{\pi}{4}\ \phi^2 = \rho\ \frac{\pi}{6}\ \phi^3\ A$$

where

q = dynamic pressure based on the slip velocity

C_D = drag coefficient

ρ = liquid density

A = acceleration

leaving

$$\phi = 1.5\ \frac{q\ C_D}{A} \qquad (4)$$

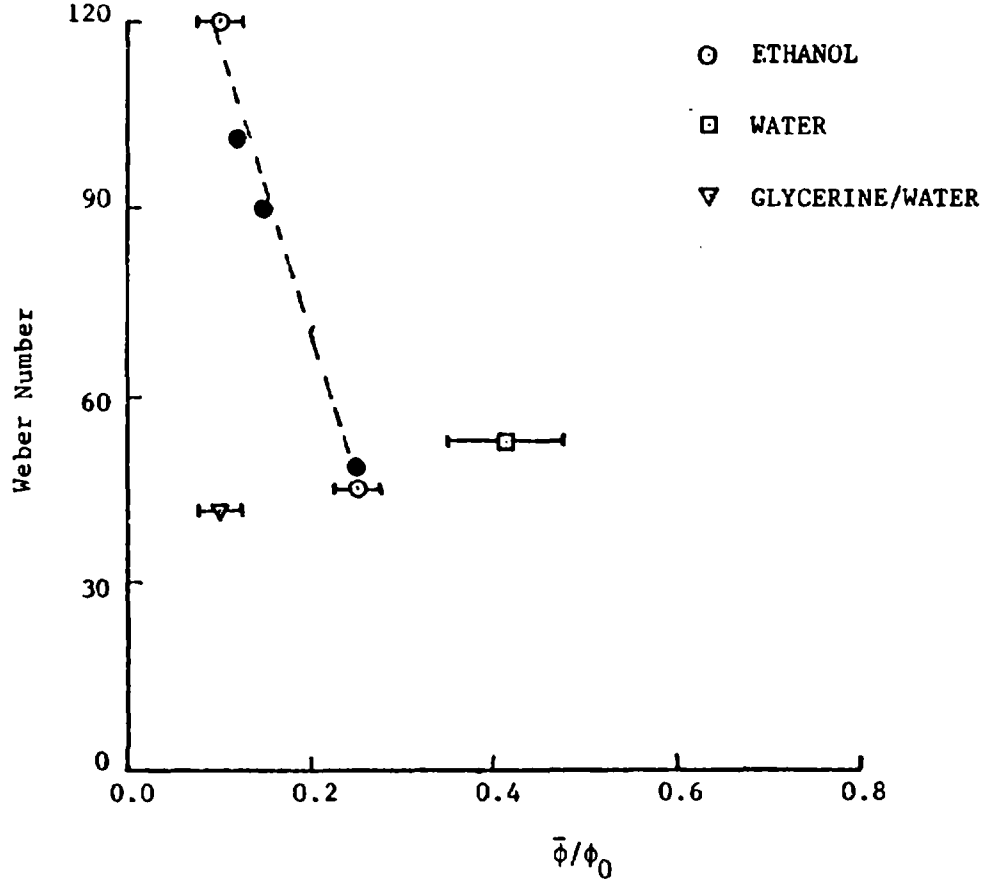

Figure 11. Mean Fragment Size Dependence on Peak Weber Number and Liquid Type: Open Symbols = LDV Data; Closed Symbols = Holography Data

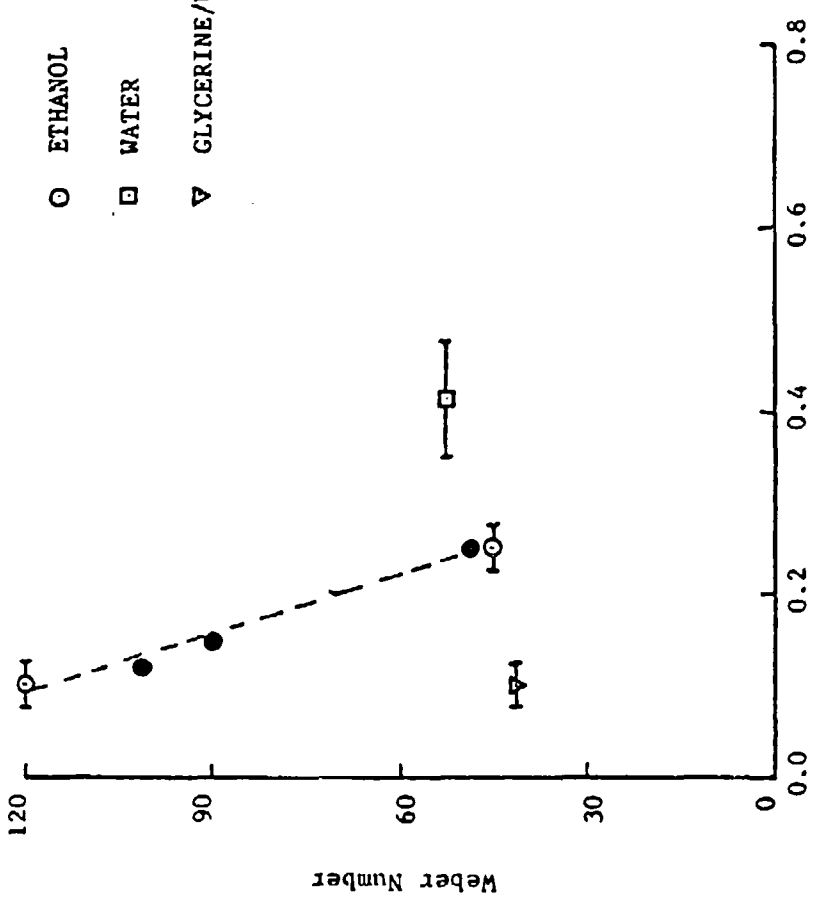

Figure 11. Mean Fragment Size Dependence on Peak Weber Number and Liquid Type: Open Symbols = LDV Data; Closed Symbols = Holography Data

For the alcohol droplets both estimates of the droplet size were in agreement. The fragment size for water and glycerine/water mixtures are also plotted; however no imaging data was available for comparison. The large fragment size estimated for water droplets was not expected and may indicate that perhaps the larger fragments were not spherical. The small fragment size for glycerine/water mixture may be a result of the initial droplet expansion to about seven times original diameter and, therefore, the bag membrane thickness must be reduced. Hence, the effect of increased liquid viscosity was reduced fragment size.

4.0 LIQUID METAL EXPERIMENTS

A series of experiments were designed to investigate the breakup dynamics of high surface tension liquid metals. Many liquid metals were identified, but mercury was selected as it was compatible with the droplet generation technique, and with room temperature air experiments. The aerodynamics of the experiment were based on trajectory estimates for mercury droplets from 100 to 600 μm. Since the liquid-to-gas density ratio was so large, the droplet velocities were assumed to be small and the slip velocity was taken as the gas velocity. This fact was verified in the experiments when the droplet velocity was limited to less than 10 percent of the gas velocity. For breakup (We = 30.), the slip velocity or gas velocity requirement ranged from 270 m/s to 109 m/s for droplet diameters of 100 μm to 600 μm, respectively. A series of experiments were defined in which the nozzle would be operated at sonic velocity and the droplet size would be varied. The 2-dimensional nozzle exhaust duct was modified to achieve sonic velocity in the throat. The nozzle would start and was operated at a stagnation pressure of 1.84×10^5 N/M^2. A droplet generator with a 130 μm diameter orifice was operated at 10 kHz and 1.5 kHz, to produce 190 μm and 300 μm diameter droplets, respectively; and a second orifice size (ϕ = 190 μm) was operated at 840 Hz to produce 560 μm diameter droplets. The test matrix is shown in Table II. The pulsed laser holography was used to record droplet images in various states along the nozzle.

4.1 Results

The droplet breakup process was very similar for the three droplet sizes, except that the breakup moved to a higher gas velocity position in the nozzle for smaller droplets. The breakup mechanism (Figure 12) is observed to be the Umbrella Mode characteristic of the Weber number range of 70-100 for conventional liquids. In this breakup mode, the droplet initially flattens and then expands to larger dimension (3-5X) forming the stem in the center and a sheet between the stem and the outer ring. The sheet bursts quickly constituting the primary breakup event. The outer ring fragments soon after the sheet bursts. The stem is stable at this point and remains secure until a higher slip velocity is reached. The sheet and ring fragments are much smaller and accelerate away from the massive stem (Figure 13). The stem is rather cylindrical and aligned with the flow. The frontal diameter of the stem is about 30-40 percent of the original droplet size and deforms as higher velocities are reached in the nozzle. Secondary breakup (Figure 12) is observed as the stem approaches the throat. The primary fragments travel downstream of the stem during the secondary breakup cycle, and at the throat the most distant fragments (which are also the smallest) are about 25. mm downstream of the stem. Finally, after the stem has failed, the breakup is essentially complete and most of the smaller fragments are spherical. The larger fragments arise from the stem and ring and the smaller fragments arise from the sheet.

The velocity and Weber number profiles (Figure 14) depict the velocities of the initial droplet, the primary fragments, and the

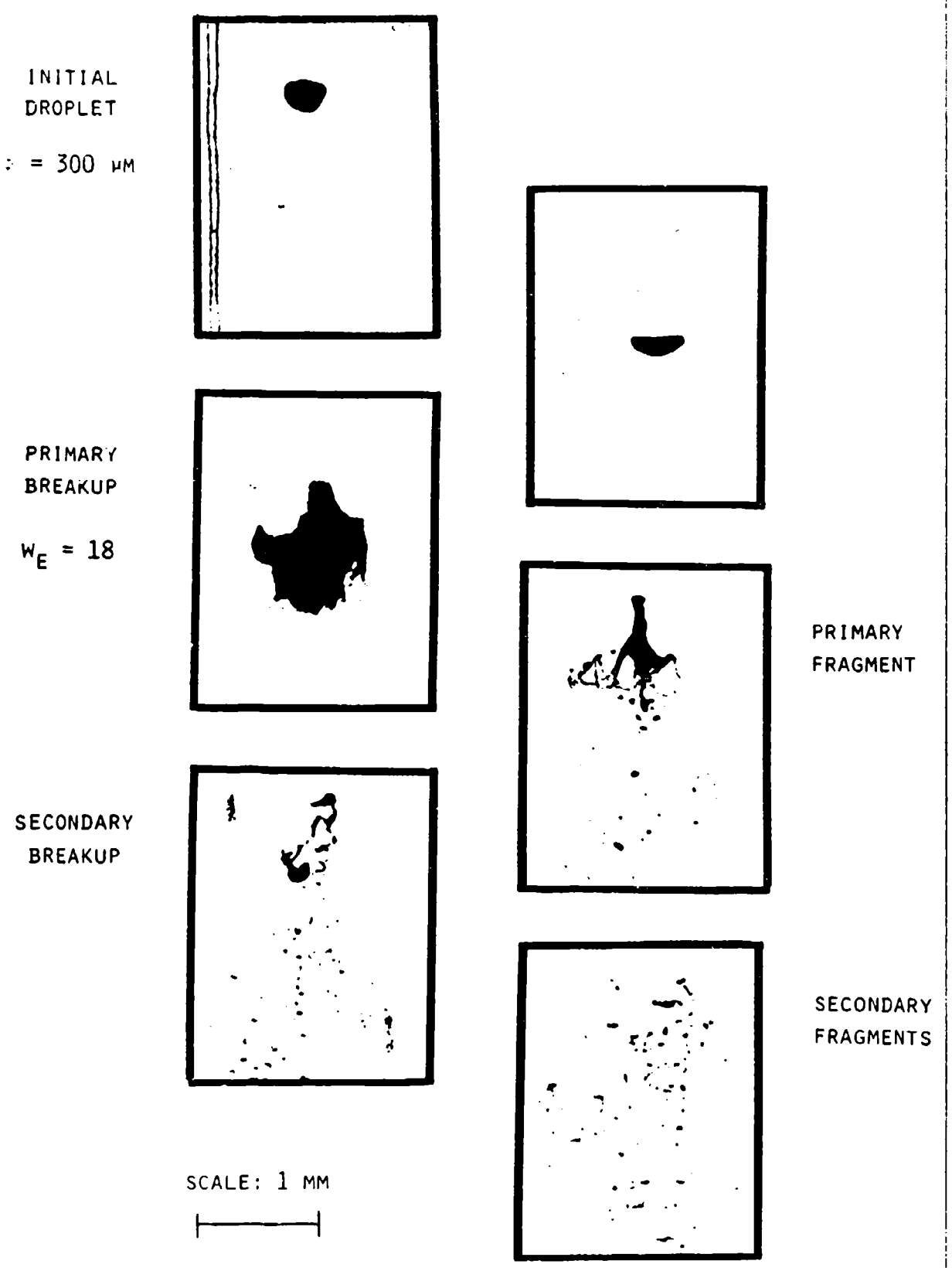

Figure 12. Metal Droplet Breakup (Series 10, Table II)

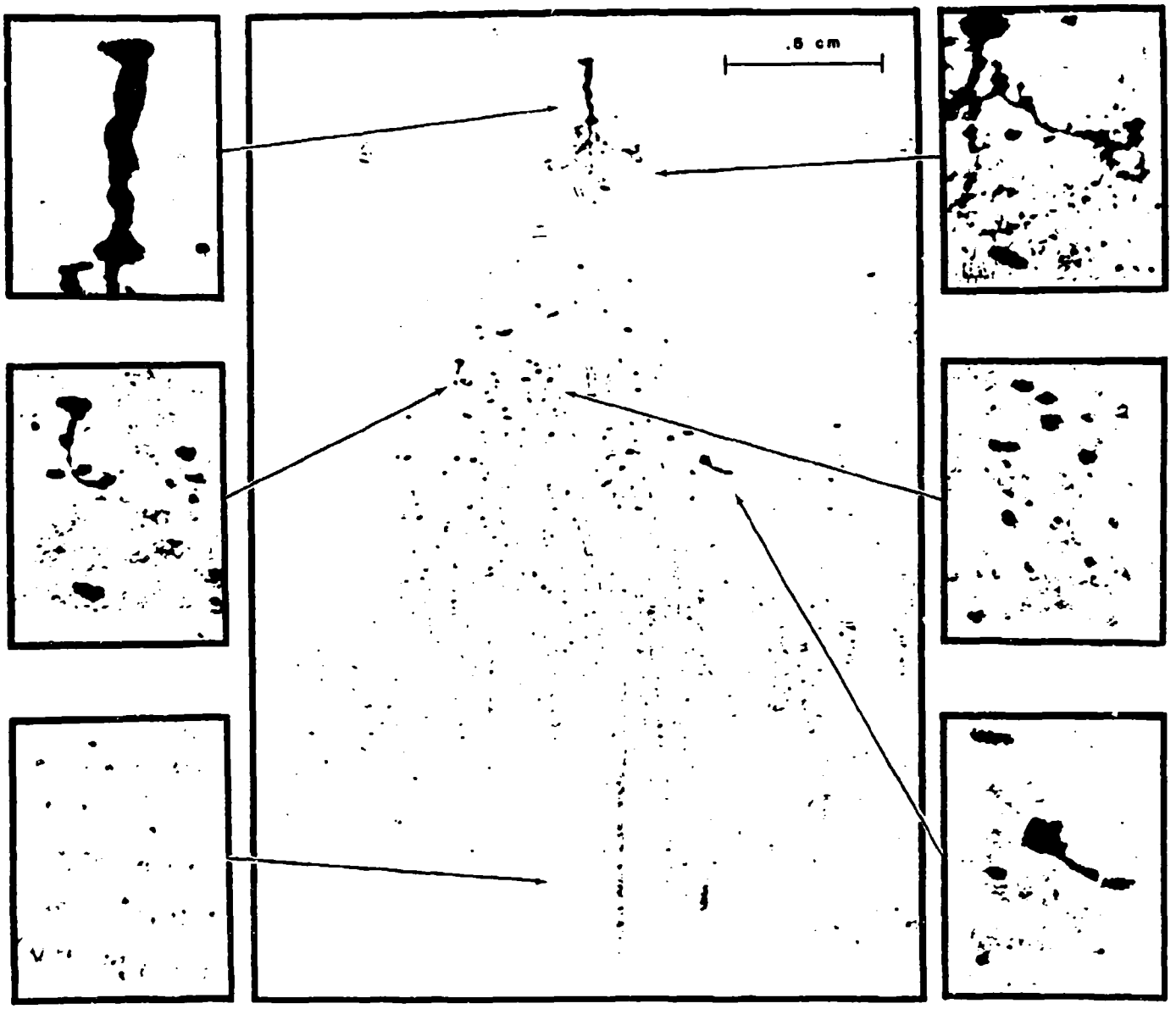

Figure 13. Primary Fragments Resulting from Metal Droplet Breakup (Series 11, Table II)

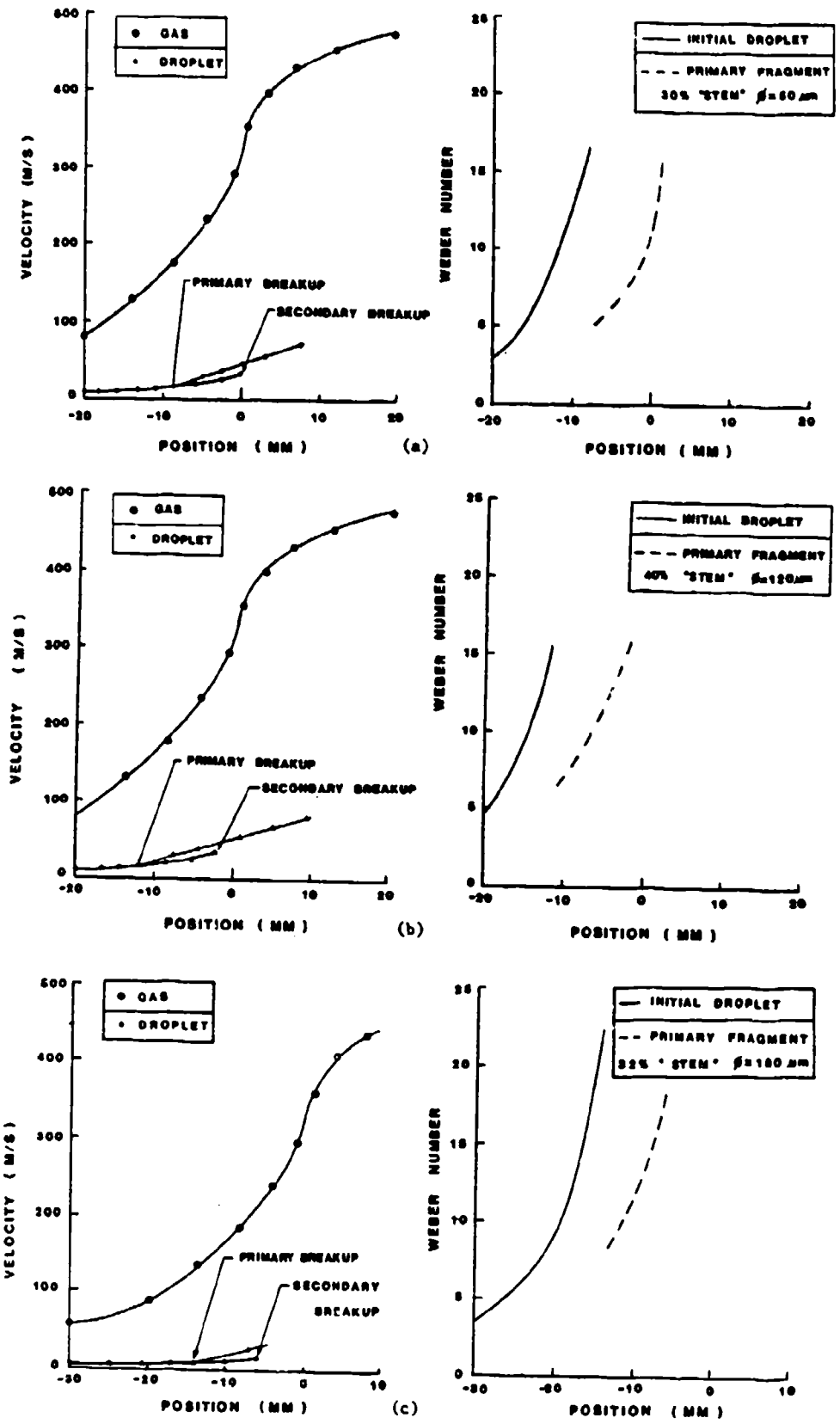

Figure 14. Metal Droplet Velocity and Weber Number Profiles: (a) Series 9, (b) Series 10, and (c) Series 11 (Table II)

stem. The position (upstream of the throat) for the primary breakup moves from 8.0 mm to 14.0 mm for the initial droplet sizes, 190 μm to 560 μm, respectively. The Weber number is based on the slip velocity and initial droplet size; then, for the stem, the Weber number is based on an approximate frontal diameter (typically $\phi_s \simeq .30\ \phi_o$). The initial droplets all fail in the Weber number range of 15-20, and the stems fail in a similar range. The Weber number histories (Figure 15) of all three sizes overlap to within the accuracy of the data, when the time is normalized by the period of the first natural frequency (Eqn. 2). This period for acoustic oscillation and the breakup time are essentially equivalent.

The fragment size distribution was determined from high magnification photographs of the reconstructed holographic images (ten events were sampled.). An estimate of the equivalent spherical diameter was used for nonspherical fragments. The fragment number density distribution (Figure 16) ranges from 5-50 μm and the sampling volume for each droplet size bin is corrected for the depth of field. The mean fragment size is about 10 percent of the original droplet diameter. Each fragment number density/size distribution is a result of a single droplet breakup event in the nozzle contraction. The sample is obtained in an instant in time, but is spatially averaged along the nozzle.

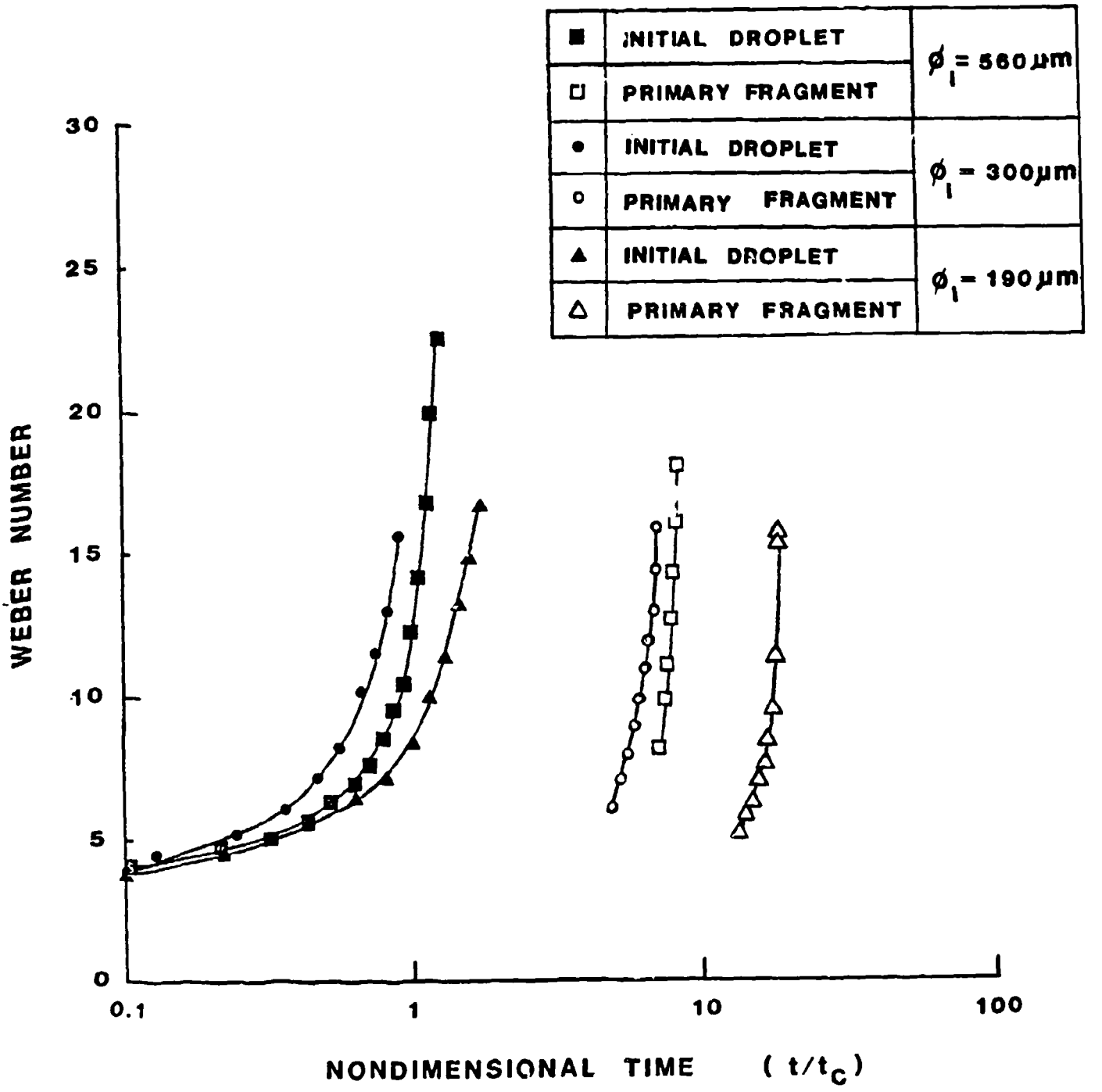

Figure 15. Metal Droplet Weber Number Histories

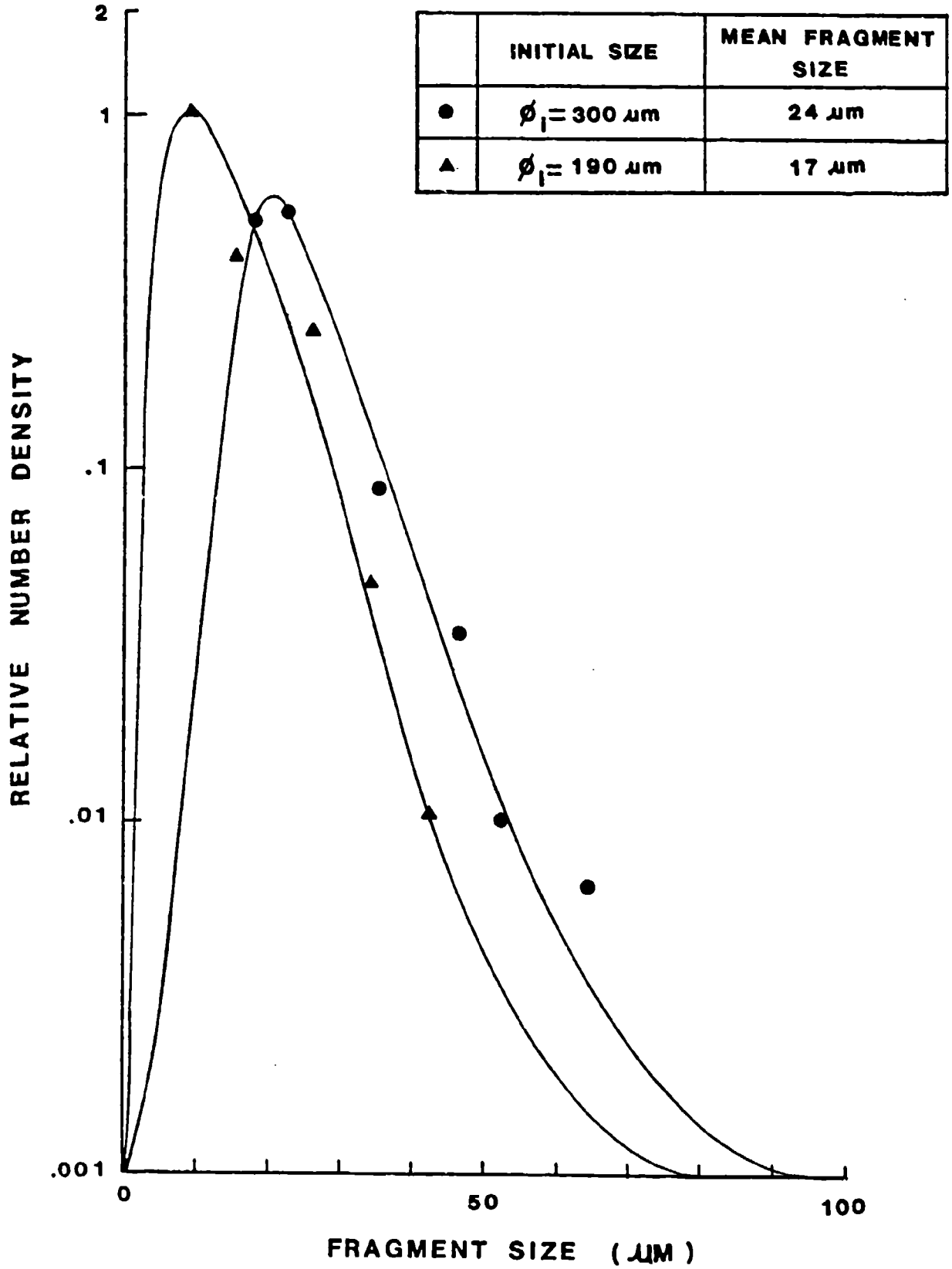

Figure 16. Fragment Number Density/Size Distribution

5.0 SUMMARY

Droplet breakup experiments have been performed in laboratory scale nozzle contraction (throat size ≈ 12 mm square). Room temperature air was used for the test gas and a conventional liquid and a liquid metal was used to produce the droplets. The droplet size was varied from 100 μm to 600 μm and the nozzle velocity rise was varied from 100 m/s to 300 m/s. Droplet velocity profiles along the nozzle were resolved with laser velocimetry and with double pulsed laser holography which also provided graphic images of the droplet breakup mechanisms and of the droplet fragments. The droplet velocity profiles were used to determine the Weber number profiles and histories. Thus, the critical Weber number and a measure of the duration of the droplet breakup event was determined.

The breakup mechanism for conventional liquid droplets was, in general, equivalent to the Bag type previously observed in shock tube experiments. The critical Weber number and breakup time data revealed that when breakup occurs in a short time that higher Weber numbers are required; and conversely when breakup occurs in a long time that lower Weber numbers are required. This trend was observed for both water and alcohol droplets. For water droplets we observed a critical Weber number of about 50 for breakup times of about 2-4 which then decayed to a data point for which breakup did not occur in the nozzle contraction. One of the alcohol data points fell on the water boundary, while the others reached the highest critical Weber numbers observed in these experiments. The data obtained for the more viscous liquid

(a glycerine/water mixture) revealed the effect of increased viscosity to be increased acceleration. Viscous liquid droplets were observed to flatten to almost seven times their original diameter before breakup occurred. The increased acceleration resulting from the larger cross section reduces the slip velocity or Weber number achieved within the nozzle. An additional effect of increased viscosity is a reduction in the fragment size. The ratio of the mean fragment to initial droplet size was determined for various Weber number failures. For alcohol and water droplets, the ratio varied from 40% at low Weber number, 50, to about 10% at high Weber number, 120. Interesting, the high viscosity data point reveals a fairly small fragment size for the low Weber number, 40.

The liquid metal droplet experiments required higher dynamic pressures for breakup and as a result the nozzle was operated at the sonic velocity. The breakup mechanism was observed to be the "Umbrella" type. This mechanism has been observed for mercury droplets in shock tube experiments, but only for Weber numbers over 80. The breakup mechanism for lower Weber number shock tube experiments "Bag" type. A large stem resulted from all primary breakup events which eventually failed further down the nozzle as higher slip velocities are achieved. Secondary breakup is an important feature of the metal droplet breakup mechanism. In contrast to the conventional liquid results, the Weber number histories for liquid metals collapsed to a single curve terminated by the primary breakup event. All three droplet sizes experienced breakup at the same Weber number, 20. Also, the duration of the breakup event was observed to be a constant when normalized by the

natural period. The fragment size distribution was observed to have a mean value of about ten percent the original droplet size. Since the critical Weber number did not vary one might expect the relative mean fragment size not to vary.

6.0 REFERENCES

1. Gilbert, M., L. Davis, and D. Altman, Jet Propulsion, Vol. 25 (1955).

2. Kliegel, J. R., "Gas Particle Nozzle Flows", Ninth Symposium (International) on Combustion, Academic Press (1963).

3. Kliegel, J. R. and G. R. Nickerson, "Axisymmetric Two-Phase Perfect Gas Performance Program, Vol. I", NASA CR 92069, April 1967.

4. Coats, D. E., et al, "A Computer Program for the Prediction of Solid Propellant Rocket Motor Performance, Vol. 1", AFRPL-TR-75-36, July 1975.

5. Penny, M. M., et al, "Supersonic Flow of Chemically Reacting Gas-Particle Mixtures, Vol. II: RAMP, A Computer Code for Analysis of Chemically Reacting Gas-Particle Flows", LMSC-HREC TR D496555-II, Lockheed Missile and Space Company, Huntsville, AL, January 1976.

6. Brundige, W. N. and L. H. Caveny, "Combustion of Low Burn Rate HTPB Propellants in the Acceleration Field", 16th JANNAF Combustion Meeting, CPIA Publication 308, III (1979).

7. Gany, A., L. H. Caveny, and M. Summerfield, "Aluminized Solid Propellants Burning in a Rocket Motor Flowfield", AIAA Journal, Vol. 16, July 1978.

8. Crump, J. E., J. L. Prentice, and K. J. Kraeutle, "Role of Scanning Electron Microscope in the Study of Solid Propellant Combustion: II. Behavior of Metal Additives", Combustion Science and Technology, Vol. 1, November 1969, pp. 205-223.

9. Boggs, T. L. et al, "Combustion of Solid Propellants and Low Frequency Combustion Instability Progress Report", Naval Weapons Center, China Lake, Ca. NWC TP4749, June 1969.

10. Crump, J., "Behavior of Aluminum in Composite Propellants in Combustion of Solid Propellants and Low Frequency Combustion Instability", Naval Weapons Center, China Lake, Ca., NOTS TP4244, June 1967.

11. Radke, H. H., L. J. Delaney, and P. Smith, "Exhaust Particle Size Data from Small and Large Solid Rocket Motors", Report No. TOR-1001 (S2951-18)-3, Aerospace Corporation, Contract AF04(695)-1001, July 1967.

12. Willoughby, P. G. and R. L. Carlson, "Sampling and Size Determination of Particles from the Titan III-C Exhaust Plume", TR-33-74-U1, United Technology Center, February 1974.

13. Strand, L. D. and G. Varsi, "Airborne Measurements of Particulates from Solid Rocket Boosters", JANNAF 8th Plume Technology Meeting, CPIA Publication 257, September 1974, pp. 141-163.

14. Dawbarn, R., "Species in Solid Rocket Exhausts", Triannual Progress Report, V34P-AIA, Inc., January 1977.

15. Strand, L. D., et al, "Characterization of the Exhaust Particulates in the Ground Cloud and High Altitude Plume of Large Solid Propellant Booster Rockets", AIAA Paper No. 80-0354, January 1980.

16. Caveny, L. H. and A. Gany, "Breakup of Al/Al_2O_3 Agglomerates in Accelerating Flowfields", AIAA Journal, Vol. 17, No. 12, December 1979.

17. Haas, F., "Stability of Droplets Suddenly Exposed to a High Velocity Gas Stream", A.I. Ch. E. Journal, Vol. 10, No. 6, pp. 920-924, November 1964.

AIAA-84-0201

Conventional and Liquid Metal Droplet Breakup in Aerodynamic Nozzle Contractions

J.E. Craig, Spectron Development Labs.,
Costa Mesa, CA

AIAA 22nd Aerospace Sciences Meeting

January 9-12, 1984/Reno, Nevada

CONVENTIONAL AND LIQUID METAL DROPLET BREAKUP IN AERODYNAMIC NOZZLE CONTRACTIONS

J. E. Craig*
Spectron Development Laboratories, Inc.
Costa Mesa, California

Abstract

The breakup of AL/AL_2O_3 agglomerates in solid propellant rocket nozzles is a critical process effecting combustion efficiency and two-phase flow losses. Droplet breakup experiments in aerodynamic nozzle contractions have been conducted in which conventional liquids and higher surface tension liquids (mercury) were examined. Pulsed laser holography has provided droplet and fragment observations with resolution not previously obtained. Laser velocimetry has provided droplet dynamics data revealing dramatic accelerations prior to breakup. Conventional liquid droplets were observed to survive to much higher Weber numbers (of order 100) than those considered to be critical for breakup. In contrast, the liquid metal droplets were observed to fail at fixed Weber number of about 15-20 and the duration of the failure event was found to scale with a time scale based on the liquid properties.

Introduction

Combustion efficiency of aluminized propellants in solid rocket motors is reduced by incomplete aluminum combustion and two-phase nozzle flow losses. The combustion of aluminized propellants can produce large Al/Al_2O_3 agglomerates. The agglomerate dynamics within the combustion chamber and nozzle have a significant influence on the overall combustion efficiency of the motor[1-5]. Agglomerates are subjected to large aerodynamic loads within the rocket nozzle where the gas phase experiences a more rapid acceleration than the agglomerates. The drag load deforms the agglomerates and if of sufficient magnitude result in breakup. The smaller fragments have faster velocity and thermal equilibrium times and have higher combustion rates. For maximum combustion efficiency the aluminum fragments must completely oxidize, and achieve kinetic and thermal equilibrium with the gas phase. As a direct result of agglomerate breakup, the aluminum combustion rate is increased, and the thermal energy released is more efficiently transferred into exhaust kinetic energy.

Photographic observations obtained in windowed rocket motors[6-7] and combustion bombs[8-10] indicate relatively large agglomerates (100μm - 500μm) are formed on the propellant surface and entrained in the combustion flow; however, particle size measurements obtained from sampling the exhaust plumes[11-15] indicate small mean particle diameters (<10μm). These small exhaust plume particles apparently result from the breakup of the larger agglomerates during the nozzle expansion process. Observations of agglomerate breakup in a laboratory scale rocket nozzle revealed an adequate correlation with Weber number; however, neither the physical process of breakup nor the fragment size distribution was resolved[16].

This research has the objective of obtaining physical data to characterize the mechanisms of aerodynamic droplet breakup. An experiment has been completed in which conventional liquids (water, alcohol and glycerine/water mixtures) and a liquid metal (mercury) was studied. The primary goal of the conventional liquid experiments was to examine the effect of liquid properties (viscosity and surface tension) on the breakup mechanism, time scale, and fragment size distribution. The goal of the liquid metal experiments was to examine the effect of the much higher surface tension more characteristic of liquid aluminum.

A key element of the experimental effort is the use of nonintrusive laser diagnostics including pulsed laser holography and laser Doppler velocimetry. The exceptional temporal and spatial resolution of pulsed laser holography provided the ability to resolve the mechanism of breakup and the size distribution of the fragments. Laser Doppler velocimetry was used to determine drop velocity distributions along the nozzle revealing the rapid acceleration of the flattened droplets and then surprisingly the milder acceleration of the fragments. The high drag to mass ratio of the flattened droplets was expected and resolved during the initial phase of the breakup process.

Experiment Considerations

Aerodynamic droplet breakup is characterized by the magnitude and duration of the aerodynamic forces. For nozzle contractions, the droplets are loaded as a result of the higher gas phase acceleration. The droplets respond to the aerodynamic forces by deforming and accelerating. The initial acceleration scales with the initial diameter; however, as the pressure forces flatten the droplet, increasing its cross-sectional area, the drag load and the acceleration increases rapidly. This sequence of events can, of course, lead to catastrophic deformation and droplet breakup if the slip velocity is of sufficient magnitude and duration.

The liquid surface tension is used to scale the aerodynamic load forming the Weber number:

$$We = \frac{\rho \, \Delta v^2 \, \phi_d}{\sigma_d} \qquad (1)$$

ρ = density
Δv = slip velocity
ϕ = diameter
σ = surface tension

*Member AIAA

The duration of the aerodynamic loading can be scaled by the natural period for hydrodynamic oscillation, which is a measure of the droplet response time:

$$\tau_n = \left(\frac{\rho_d \phi_d^3}{\sigma_d}\right)^{1/2} \quad (2)$$

For nozzle accelerations, an additional time scale exists; namely the time required for velocity equilibrium, τ_v. Assuming the droplet Reynolds number relative to the gas phase is sufficiently high (i.e., $Re > 10^3$), the drag coefficient for rigid droplets is approximately unity and the corresponding time scale is

$$\tau_v = \frac{\rho_d \phi_d}{\rho \Delta v} \quad (3)$$

However, since the liquid droplets are not rigid, the droplet cross section and the associated drag load increase rapidly within the nozzle contraction. Therefore, the time scale for liquid droplet velocity equilibrium is no doubt faster than the rigid droplet estimate.

A few liquid types were selected to examine the effect of liquid properties such as surface tension and viscosity. For the conventional liquids, water and alcohol were selected for the surface tension series; and water and a glycerine water (57/43) mixture were selected for the viscosity series. The mixture was selected to achieve a viscosity ten times that of water.

A second series of experiments were designed to examine the breakup dynamics of high surface tension liquid metals. Mercury was selected because of its compatibility with the droplet generation technique and with room temperature air flow.

Nozzle Facility

An experiment was designed in which droplet breakup could be investigated in a nozzle contraction. The nozzle was designed to allow droplet injection upstream of the contraction. Windows formed the sides of the two-dimensional nozzle allowing observation of the droplet interaction. The gas was delivered from a settling chamber through a sintered metal throttle to the nozzle plenum where the droplets were injected. The nozzle area ratio was eight, Fig. 1. For the conventional liquid experiments, the nozzle was operated at subsonic exit velocities. However, for the liquid metal experiments, high dynamic pressures were required to achieve droplet breakup. Higher droplet loading was achieved by increasing the gas velocity and hence the slip velocity. In fact, the nozzle exhaust was modified to allow sonic flow in the nozzle throat for the liquid metal experiments, although droplet breakup occurred upstream of the throat.

Piezoelectric droplet generators were constructed to produce highly monodisperse droplet streams. The basic design was that of modern ink-jet printers. The complete droplet generator is composed of a liquid supply tank, an electrical driver, and the ink-jet devices (Figure 1). The size of the droplets generated by our devices was variable from about 1.5 to 3.0 times the orifice diameter by decreasing the excitation frequency. For conventional liquids, droplets were generated from 160 μm to 400 μm in diameter, and for mercury, droplets were generated from 190 μm to 560 μm. The droplet generator operating conditions are listed in Table I for the conventional liquids and mercury.

TABLE I. DROPLET GENERATOR OPERATING CONDITIONS

LIQUID	DIAMETER		EXCITATION FREQUENCY (kHz)
	TIP (μm)	DROPLET (μm)	
Water	100	160	10.6
	120	220	8.0
	190	410	0.8
Alcohol	100	164	11.2
	150	265	9.0
Glycerine/ Water	120	240	7.2
Mercury	130	190	10.0
	130	300	1.5
	190	560	0.8

Droplet Holography

Holographic observations of the droplet interaction within the nozzle contraction were produced. The holocamera imaging optics were configured with object-to-hologram image magnifications of one and five. The large field-of-view optics (ϕ = 100 mm diameter, 1x magnification) were used in the initial experiments in which the droplet velocities were measured along the nozzle. Double exposure (Δt=10μs) holography is used to observe droplet velocity. Smaller field-of-view optics (ϕ = 25 mm diameter, 5x magnification) were used to record high resolution observations of the droplet breakup process. For this case, external triggering was required to center the droplet position in the hologram. With premagnification (5x) the holocamera spatially resolves 4μm in reconstruction. Since the holograms are recorded in 10^{-8} seconds, droplets of order 10μm diameter can be resolved at velocities approaching 10^3 m/s. For these experiments the droplet velocities were limited to about 100 m/s.

Laser Velocimeter

Droplet and gas phase velocities were obtained using laser Doppler velocimetry (LDV). This technique is based on laser light scatter by droplets or seed particles in the flow. A single laser beam (Spectra Physics, Model 124, 15 m watt) is split into two equal intensity beams which intersect at the desired measurement point in the flow. Electromagnetic interference between the two laser beams occurs at the intersection region resulting in fringe formation. The fringes are parallel planes of high intensity (constructive interference) alternating with lower intensity

TABLE II. TEST MATRIX

SERIES	LIQUID	DROPLET (μm)	GAS VELOCITY (m/s)	SLIP VELOCITY (m/s)	WEBER NUMBER	BREAKUP TIME (ms)	NATURAL PERIOD (ms)
1	Water	140	100	82	17	2.25	0.20
2		160	190	135	53	0.9	0.25
3		410	100	78	49	2.2	1.0
4		410	190	84	56	1.7	1.0
5	Alcohol	165	100	77	58	1.3	0.40
6		176	190	105	110	1.6	0.44
7		265	160	80	93	1.5	0.82
8	Glycerine, 57% Water, 43%	240	170	88	33	0.93	0.44
9	Mercury	190	310	165	17	0.77	0.45
10		300	310	135	16	0.80	0.89
11		560	310	119	22	2.8	2.3

(destructive interference). For these experiments the spacing between successive fringes was 7μm. Light scattered by particles in the flow produces signals modulated by the fringe pattern intensity. The electronic signal processor (Macrodyne, 2000 Series, LDV Processor) measures the time between successive fringes from which particle velocity is obtained. Distributions of a large number of events (typically 10^4) were obtained at each measurement point in the flow from which mean velocities were obtained. The droplet and fragment velocity distributions were measured with the laser velocimeter. The mean velocity is calculated at each station. The droplet velocity profile was integrated to determine the elapsed time and differentiated to determine the acceleration. The gas/droplet slip velocity was used to determine the Weber number (based on initial droplet diameter) history along the nozzle. Hence, both the Weber number at droplet breakup and the breakup time were determined.

Conventional Liquid Experiments

A series of experiments were conducted to observe the droplet deformation and fragmentation processes with holography and to determine the droplet and fragment dynamics with laser velocimetry. The experiments were conducted with three liquid types. For each liquid with a corresponding surface tension, a parametric set of trajectory calculations were performed for various nozzle exit velocities, and droplet sizes. In an early series of experiments, the rigid droplet trajectory estimates were found to grossly over estimate the Weber number history when compared to experiment data. In the experiments, the liquid droplets were found to achieve much higher accelerations just prior to breakup. The mechanism for enhanced acceleration was presumed to be droplet flattening, and as a result the droplet Weber numbers were lower than predicted. The gas velocity was increased so that breakup occurred. The test conditions are listed in Table II; including the liquid type, droplet size, maximum gas velocity, the slip velocity and Weber number at breakup, the breakup time, and the period of the first natural frequency (i.e. Eqn. 2). The breakup times were measured relative to the time at which the Weber number exceeded five.

Results

The holographic investigation revealed that the breakup mode for nozzle accelerations was similar to the breakup modes observed for shock wave accelerations. Initially the droplet flattens under the high pressure exerted on the stagnation point. As the droplet flattens, its radius of curvature increases and the stagnation pressure is felt over a larger area. The center of the droplet is eventually pushed downstream of the outer edge forming a thin membrane in the shape of a bag (Figure 2). When the bag bursts, very small fragments are formed; however, considerable mass still remains in the annular ring. The annular ring fails later producing the larger fragments as has been reported by others[17].

The laser velocimeter was used to obtain velocity distributions (Figure 3). Initially the velocity distribution is narrow; however, the distribution broadens substantially within the breakup region. Finally, as a result of the large increase in the mean velocity of the fragments the relative width of the distribution is reduced. The broad distribution within the breakup region should not be confused with turbulence, but should be associated with the breakup phenomena. Fairly mild accelerations were observed until the droplet begins to deform and flatten. The drag to mass ratio of the flattened droplet is considerably higher than for the spherical geometry; and as a result the droplet experiences extreme accelerations just before breakup. This final acceleration, of course, reduces the peak slip velocity and Weber number and must be accurately modeled if the Weber number at breakup is to be predicted.

The Weber number profiles for water droplets are shown in Figure 4. The position at which breakup occurs moves downstream if the droplet size or the nozzle velocity is reduced. As a result of reduced size or velocity the peak Weber number is reduced; and eventually, a condition is reached for which droplet breakup does not occur within the nozzle contraction. In our experiments with water droplets, this condition was reached only for the smallest droplet size, 150 μm, and the smallest velocity rise, 100 m/s, in which case, the Weber number did not exceed 20 and failure did not occur in the nozzle contraction. Thus, for a given velocity rise in the nozzle contraction, there exists a boundary in the Weber number/position plane at which droplet breakup occurs.

Since the breakup position is dependent on the nozzle velocity rise, consider instead the time history of loading. This is a more unified approach since it is the loading duration which produces droplet deformations and eventually breakup. A zero time must be selected and we have chosen the time at which the Weber number reaches five. The Weber number (loading) is plotted against relative time and different velocity rise and droplet size conditions compared. The relative time has been normalized by the period of the first natural frequency (Eqn. 2).

The water droplet data (Figure 5) fall along a boundary starting at a Weber number of about 50 and time of one and extending to very low Weber numbers at long times. One of the alcohol data points is near the water boundary, while the others are at much higher Weber numbers (i.e., over 100). The glycerine droplet data point indicates that breakup occurred at a lower Weber number than for water droplets. Holographic observations revealed that the glycerine droplets flattened to a much larger cross section as a result of the increased viscosity. The additional cross section increased the drag and acceleration resulting in a lower Weber number trajectory. The fundamental result is that gradual loadings produced by nozzle accelerations allows the droplets to reach higher Weber numbers than are critical for impulsive loading as produced in shock tube simulations.

Breakup Parameters

Weber number effect on breakup was studied by changing both droplet size and nozzle velocity. The bag was still observed to expand downstream of the ring; however, after the bag bursts, the ring exhibits more random distortion with increasing Weber number. Increased Weber number was observed to decrease the fragment size. The mean fragment size is plotted against peak Weber number (Fig.6). The mean fragment size based on acceleration (Equation 4) is also plotted. The mean fragment size was estimated by using a force balance on the fragments. The drag load was written in terms of the slip velocity, fragment size, and a drag coefficient based on the Reynolds number. The mass was written in terms of the fragment size and density (the fragments are assumed spherical, a fact confirmed by holographic data); and the acceleration was measured.

The force balance resulted in an equation for the fragment size, ϕ, as follows:

$$F = MA$$

or

$$q\, C_D \frac{\pi}{4} \phi^2 = \rho \frac{\pi}{6} \phi^3 A$$

where

q = dynamic pressure based on the slip velocity
C_D = drag coefficient
ρ = liquid density
A = acceleration

leaving

$$\phi = 1.5 \frac{q\, C_D}{A} \qquad (4)$$

For the alcohol droplets both estimates of the droplet size were in agreement. The fragment size for water and glycerine/water mixtures are also plotted; however no imaging data was available for comparison. The large fragment size estimated for water droplets was not expected and may indicate that perhaps the larger fragments were not spherical. The small fragment size for glycerine/water mixture may be a result of the initial droplet expansion to about seven times original diameter and, therefore, the bag membrane thickness must be reduced. Hence, the effect of increased liquid viscosity was reduced fragment size.

Liquid Metal Experiments

A series of experiments were designed to investigate the breakup dynamics of high surface tension liquid metals. Many liquid metals were identified, but mercury was selected as it was compatible with the droplet generation technique, and with room temperature air experiments. The aerodynamics of the experiment were based on trajectory estimates for mercury droplets from 100 to 600 μm. Since the liquid-to-gas density ratio was so large, the droplet velocities were assumed to be small and the slip velocity was taken as the gas velocity. This fact was verified in the experiments when the droplet velocity was limited to less than 10 percent of the gas velocity. For breakup (We = 30.), the slip velocity or gas velocity requirement ranged from 270 m/s to 109 m/s for droplet diameters of 100 μm to 600 μm, respectively. A series of experiments were defined in which the nozzle would be operated at sonic velocity and the droplet size would be varied. The 2-dimensional nozzle exhaust duct was modified to achieve sonic velocity in the throat. The nozzle would start and was operated at a stagnation pressure of 1.84×10^5 N/M^2. A droplet generator with a 130 μm diameter orifice was operated at 10 kHz and 1.5 kHz, to produce 190 μm and 300 μm diameter droplets, respectively; and a second orifice size (ϕ = 190 μm) was operated at 840 Hz to produce 560 μm diameter droplets. The test matrix is shown in Table II. The pulsed laser holography was used to record droplet images in various states along the nozzle.

Results

The droplet breakup process was very similar for the three droplet sizes, except that the breakup moved to a higher gas velocity position in the nozzle for smaller droplets. The breakup mechanism

(Figure 7) is observed to be the Umbrella Mode characteristic of the Weber number range of 70-100 for conventional liquids. In this breakup mode, the droplet initially flattens and then expands to larger dimension (3-5X) forming the stem in the center and a sheet between the stem and the outer ring. The sheet bursts quickly constituting the primary breakup event. The outer ring fragments soon after the sheet bursts. The stem is stable at this point and remains secure until a higher slip velocity is reached. The sheet and ring fragments are much smaller and accelerate away from the massive stem (Figure 8). The stem is rather cylindrical and aligned with the flow. The frontal diameter of the stem is about 30-40 percent of the original droplet size and deforms as higher velocities are reached in the nozzle. Secondary breakup (Figure 7) is observed as the stem approaches the throat. The primary fragments travel downstream of the stem during the secondary breakup cycle, and at the throat the most distant fragments (which are also the smallest) are about 25. mm downstream of the stem. Finally, after the stem has failed, the breakup is essentially complete and most of the smaller fragments are spherical. The larger fragments arise from the stem and ring and the smaller fragments arise from the sheet.

The velocity and Weber number profiles (Figure 9) depict the velocities of the initial droplet, the primary fragments, and the stem. The position (upstream of the throat) for the primary breakup moves from 8.0 mm to 14.0 mm for the initial droplet sizes, 190 μm to 560 μm, respectively. The Weber number is based on the slip velocity and initial droplet size; then, for the stem, the Weber number is based on an approximate frontal diameter (typically $\phi_s \approx .30\ \phi_o$). The initial droplets all fail in the Weber number range of 15-20, and the stems fail in a similar range. The Weber number histories (Figure 10) of all three sizes overlap to within the accuracy of the data, when the time is normalized by the period of the first natural frequency (Eqn. 2). This period for acoustic oscillation and the breakup time are essentially equivalent.

The fragment size distribution was determined from high magnification photographs of the reconstructed holographic images (ten events were sampled.). An estimate of the equivalent spherical diameter was used for nonspherical fragments. The fragment number density distribution (Figure 11) ranges from 5-50 μm and the sampling volume for each droplet size bin is corrected for the depth of field. The mean fragment size is about 10 percent of the original droplet diameter. Each fragment number density/ size distribution is a result of a single droplet breakup event in the nozzle contraction. The sample is obtained in an instant in time, but is spatially averaged along the nozzle.

Summary

Droplet breakup experiments have been performed in laboratory scale nozzle contraction (throat size = 1 cm square). Room temperature air was used for the test gas and conventional and liquid metal was used to produce the droplets. The droplet size was varied from 100 μm to 600 μm and the nozzle velocity rise was varied from 100 m/s to 300 m/s. Droplet velocity profiles along the nozzle were resolved with laser velocimetry and with double pulsed laser holography which also provided graphic images of the droplet breakup mechanisms and of the droplet fragments. The droplet velocity profiles were used to determine the Weber number profiles and histories. Thus, the critical Weber number was determined and a measure of the duration of the droplet breakup event.

The breakup mechanism for conventional liquid droplets was, in general, equivalent to the Bag type previously observed in shock tube experiments. The critical Weber number and breakup time data revealed that when breakup occurs in a short time that higher Weber numbers are required; and conversely when breakup occurs in a long time that lower Weber numbers are required. This trend was observed for both water and alcohol droplets. For water droplets we observed a critical Weber number of about 50 for breakup times of about 2-4 which then decayed to a data point for which breakup did not occur in the nozzle contraction. One of the alcohol data points fell on the water boundary, while the others reached the highest critical Weber numbers observed in these experiments. The data obtained for the more viscous liquid (a glycerine/ water mixture) revealed the effect of increased viscosity to be increased acceleration. Viscous liquid droplets were observed to flatten to almost seven times their original diameter before breakup occurred. The increased acceleration resulting from the larger cross section reduces the slip velocity or Weber number achieved within the nozzle. An additional effect of increased viscosity is a reduction in the fragment size. The ratio of the mean fragment to initial droplet size was determined for various Weber number failures. For alcohol and water droplets, the ratio varied from 40% at low Weber number, 50, to about 10% at high Weber number, 120. Interesting, the high viscosity data point reveals a fairly small fragment size for the low Weber number, 40.

The liquid metal droplet experiments required higher dynamic pressures for breakup and as a result the nozzle was operated at the sonic velocity. The breakup mechanism was observed to be the "Umbrella" type. This mechanism has been observed for mercury droplets in shock tube experiments, but only for Weber numbers over 80. The breakup mechanism for lower Weber number shock tube experiments "Bag" type. A large stem resulted from all primary breakup events which eventually failed further down the nozzle as higher slip velocities are achieved. Secondary breakup is an important feature of the metal droplet breakup mechanism. In contrast to the conventional liquid results, the Weber number histories for liquid metals collapsed to a single curve terminated by the primary breakup event. All three droplet sizes experienced breakup at the same Weber number, 20. Also, the duration of the breakup event was observed to be a constant when normalized by the natural period. The fragment size distribution was observed to have a mean value of about ten percent the original droplet size. Since the critical Weber number did not vary one might expect the relative mean fragment size not to vary.

Acknowledgements

Research sponsored by Air Force Office of Scientific Research (AFSC) under Contract F49620-81-C-0032, Project Officer Dr. Leonard H. Caveny. The author acknowledges the technical support of Messrs. Michael Houser, David Lee and Robert Nichols.

References

1. Gilbert, M., L. Davis, and D. Altman, Jet Propulsion, Vol. 25 (1955).

2. Kliegel, J. R., "Gas Particle Nozzle Flows", Ninth Symposium (International) on Combustion, Academic Press (1963).

3. Kliegel, J. R. and G. R. Nickerson, "Axisymmetric Two-Phase Perfect Gas Performance Program, Vol. I", NASA CR 92069, April 1967.

4. Coats, D. E., et al, "A Computer Program for the Prediction of Solid Propellant Rocket Motor Performance, Vol. 1", AFRPL-TR-75-36, July 1975.

5. Penny, M. M., et al, "Supersonic Flow of Chemically Reacting Gas-Particle Mixtures, Vol. II: RAMP, A Computer Code for Analysis of Chemically Reacting Gas-Particle Flows", LMSC-HREC TR D496555-II, Lockheed Missile and Space Company, Huntsville, AL, January 1976.

6. Brundige, W. N. and L. H. Caveny, "Combustion of Low Burn Rate HTPB Propellants in the Acceleration Field", 16th JANNAF Combustion Meeting, CPIA Publication 308, III (1979).

7. Gany, A., L. H. Caveny, and M. Summerfield, "Aluminized Solid Propellants Burning in a Rocket Motor Flowfield", AIAA Journal, Vol. 16, July 1978.

8. Crump, J. E., J. L. Prentice, and K. J. Kraeutle, "Role of Scanning Electron Microscope in the Study of Solid Propellant Combustion: II. Behavior of Metal Additives", Combustion Science and Technology, Vol. 1, November 1969, pp. 205-223.

9. Boggs, T. L. et al, "Combustion of Solid Propellants and Low Frequency Combustion Instability Progress Report", Naval Weapons Center, China Lake, Ca. NWC TP4749, June 1969.

10. Crump, J., "Behavior of Aluminum in Composite Propellants in Combustion of Solid Propellants and Low Frequency Combustion Instability", Naval Weapons Center, China Lake, Ca., NOTS TP4244, June 1967.

11. Radke, H. H., L. J. Delaney, and P. Smith, "Exhaust Particle Size Data from Small and Large Solid Rocket Motors", Report No. TOR-1001 (S2951-18)-3, Aerospace Corporation, Contract AF04(695)-1001, July 1967.

12. Willoughby, P. G. and R. L. Carlson, "Sampling and Size Determination of Particles from the Titan III-C Exhaust Plume", TR-33-74-U1, United Technology Center, February 1974.

13. Strand, L. D. and G. Varsi, "Airborne Measurements of Particulates from Solid Rocket Boosters", JANNAF 8th Plume Technology Meeting, CPIA Publication 257, September 1974, pp. 141-163.

14. Dawbarn, R., "Species in Solid Rocket Exhausts", Triannual Progress Report, V34P-AIA, Inc., January 1977.

15. Strand, L. D., et al, "Characterization of the Exhaust Particulates in the Ground Cloud and High Altitude Plume of Large Solid Propellant Booster Rockets", AIAA Paper No. 80-0354, January 1980.

16. Caveny, L. H. and A. Gany, "Breakup of Al/Al_2O_3 Agglomerates in Accelerating Flowfields", AIAA Journal, Vol. 17, No. 12, December 1979.

17. Haas, F., "Stability of Droplets Suddenly Exposed to a High Velocity Gas Stream", A.I. Ch. E. Journal, Vol. 10, No. 6, pp. 920-924, November 1964.

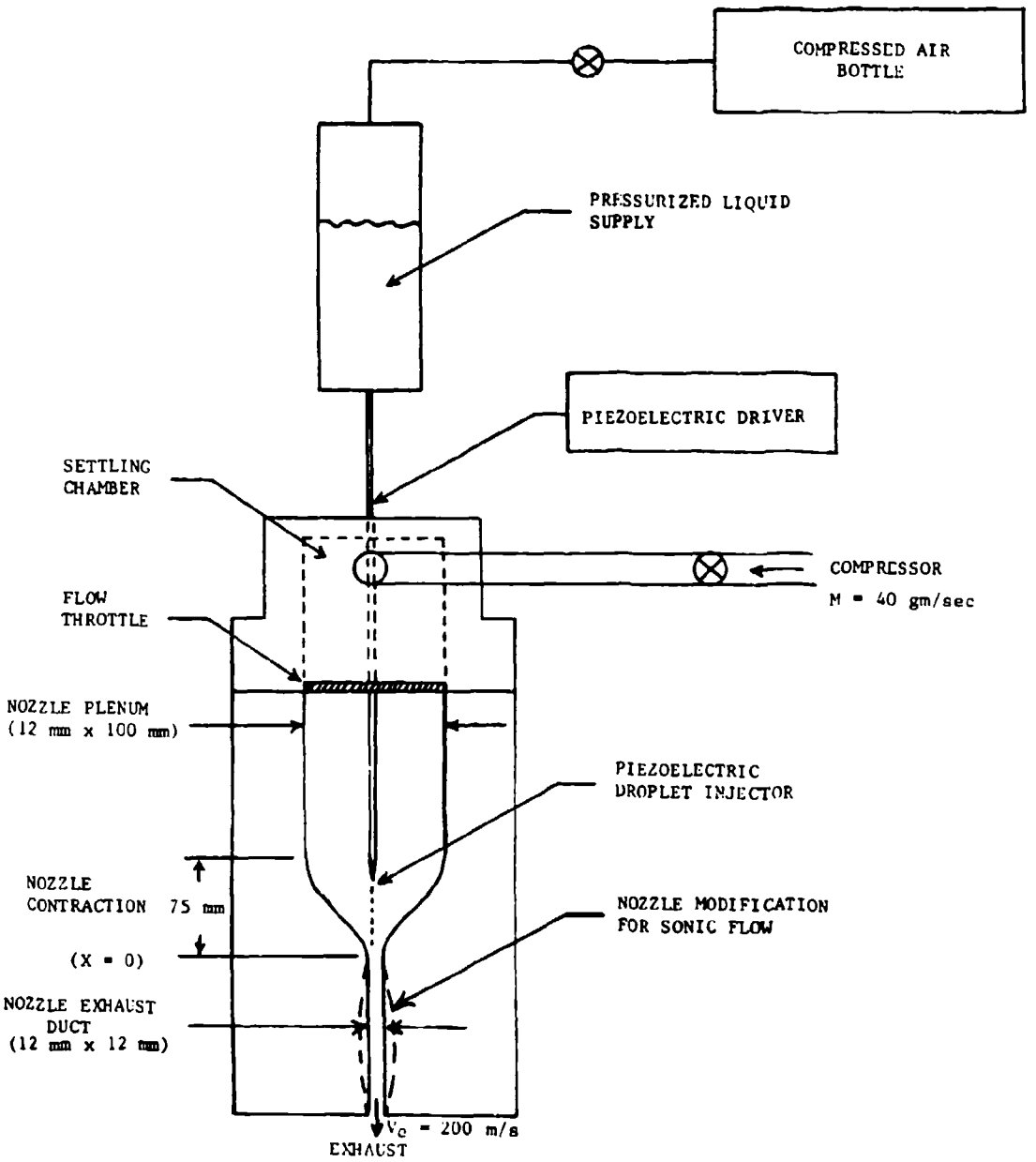

Figure 1. Nozzle Facility with Piezoelectric Droplet Injector

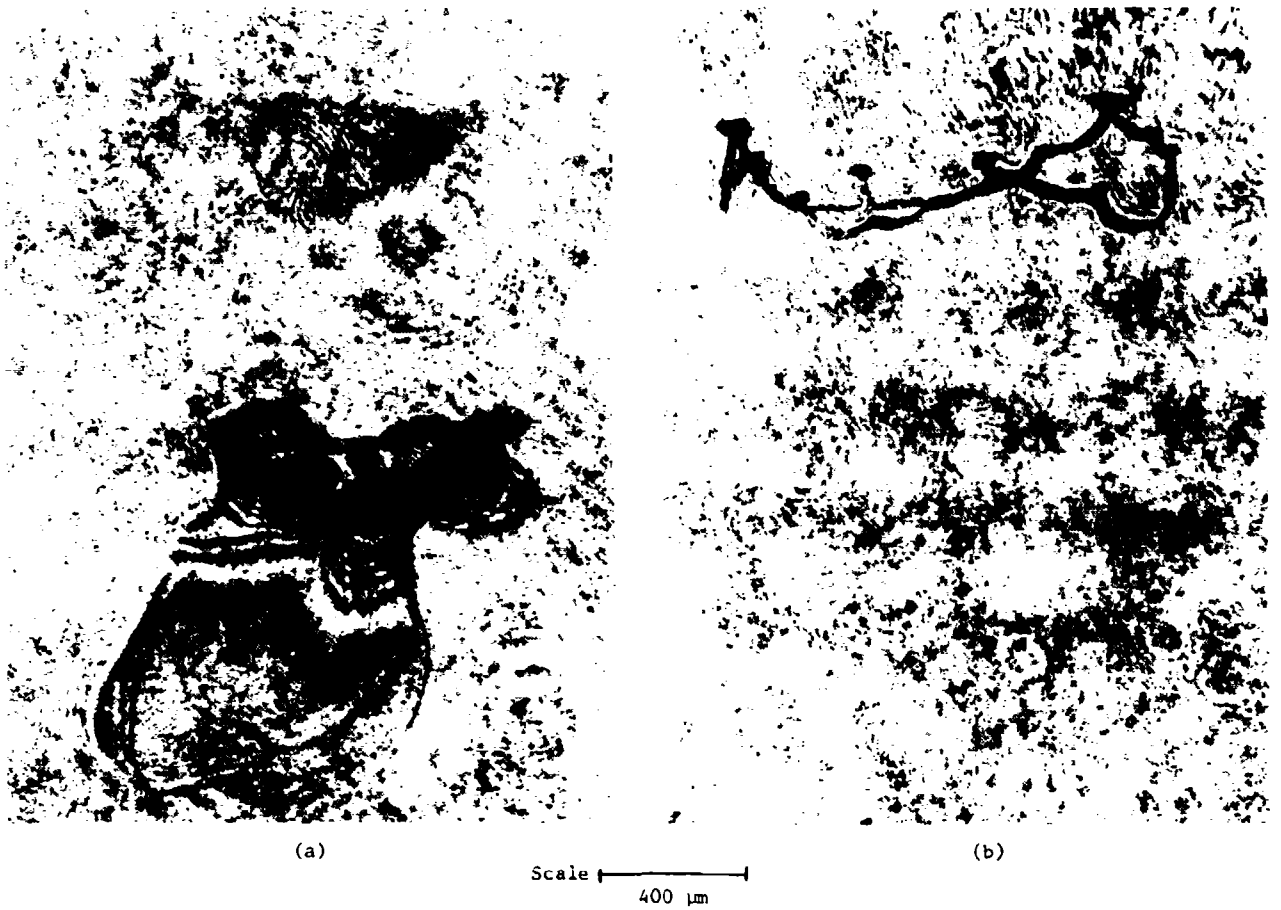

Figure 2. Holography Data, Alcohol Droplets (Series 5, Table II)
(a) Double Pulse (ΔT = 25 μs) Bag Breakup Mode
(b) Ring Structure Observed Later in Breakup Event

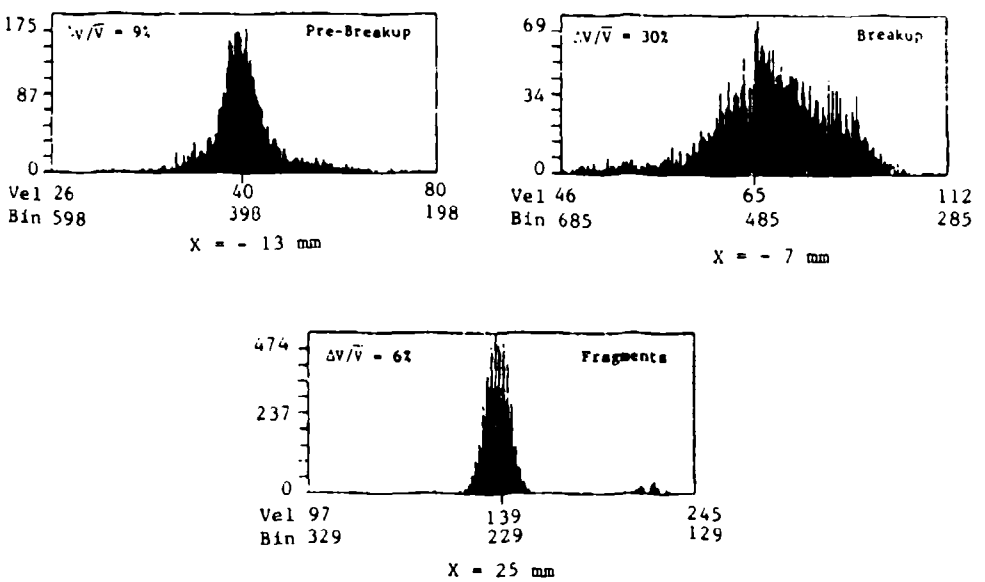

Figure 3. Laser Doppler Velocimetry Data, Point Velocity Distributions Along Nozzle (See Figure 1 for Nozzle Coordinates)

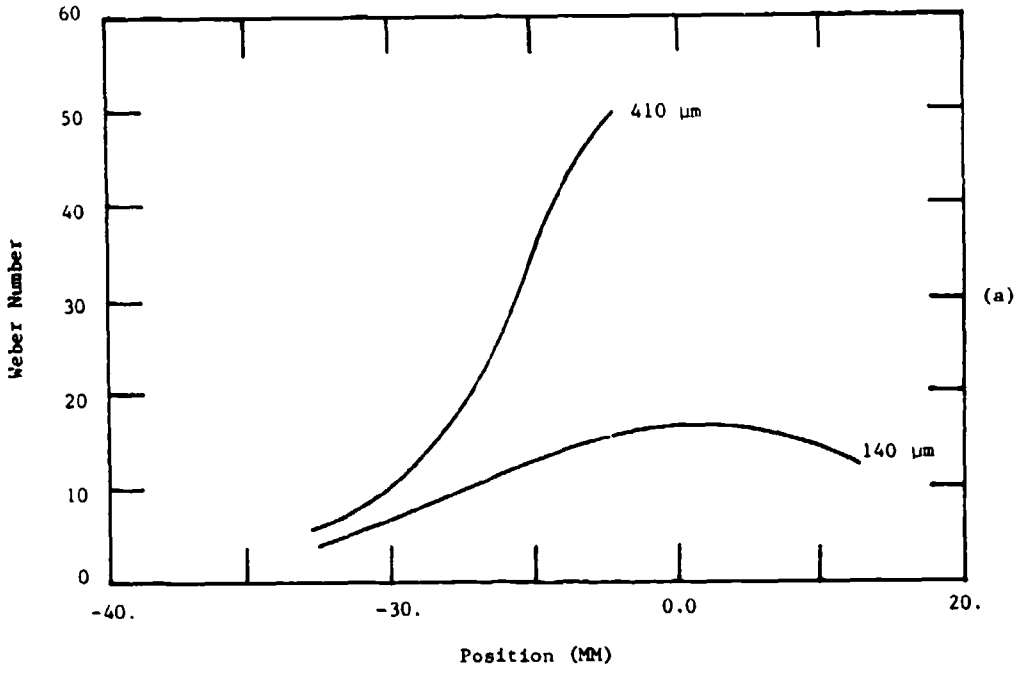

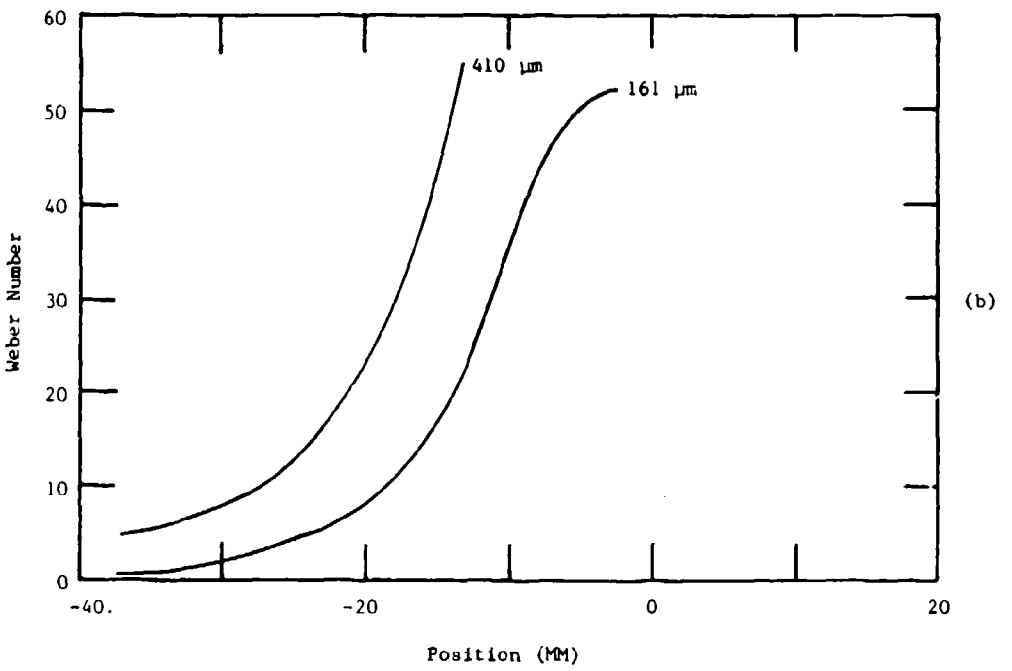

Figure 4. Water Droplet Weber Number Profiles
(Nozzle Velocity Rise; (a) 100 M/S and (b) 190 M/S)

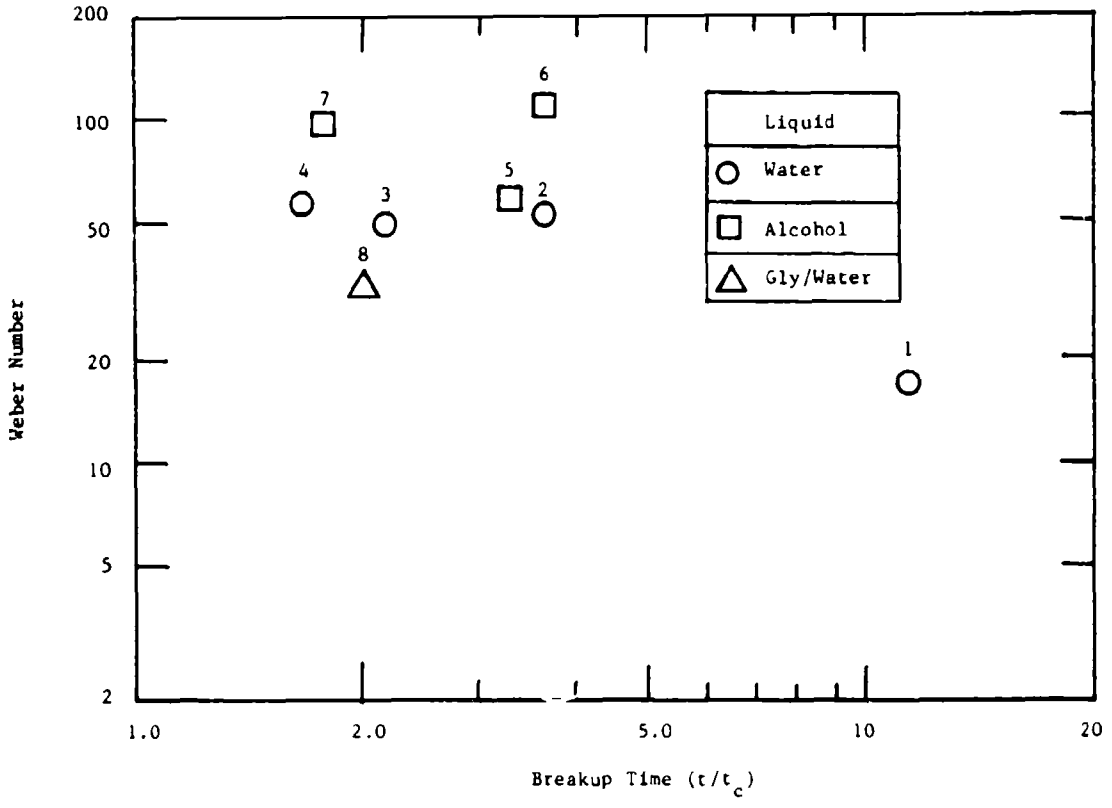

Figure 5. Critical Weber Numbers and Associated Time Durations of the Breakup Event: Series Number (i.e. 1-8) refers to Table II

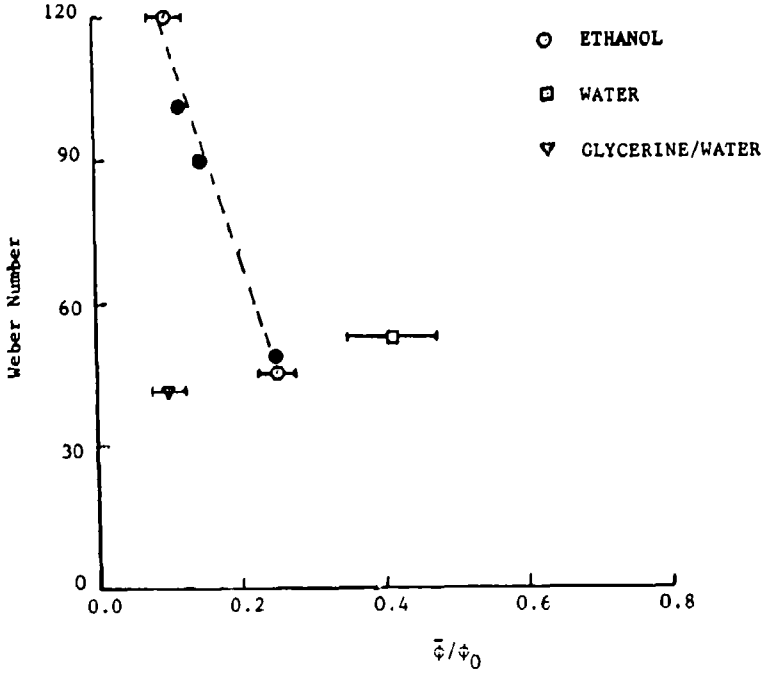

Figure 6. Mean Fragment Size Dependence on Peak Weber Number and Liquid Type: Open Symbols = LDV Data; Closed Symbols = Holography Data

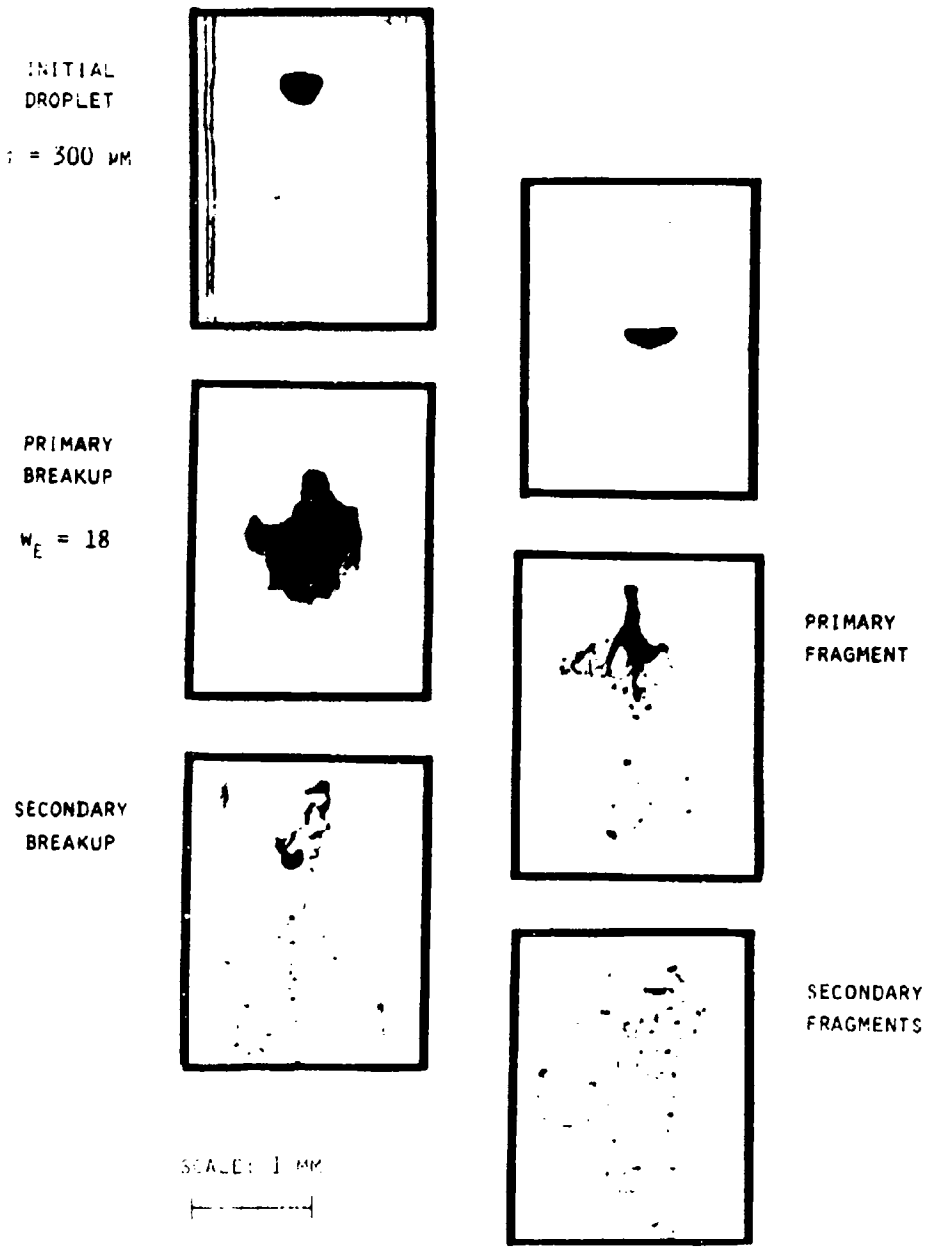

Figure 7. Metal Droplet Breakup (Series 10, Table II)

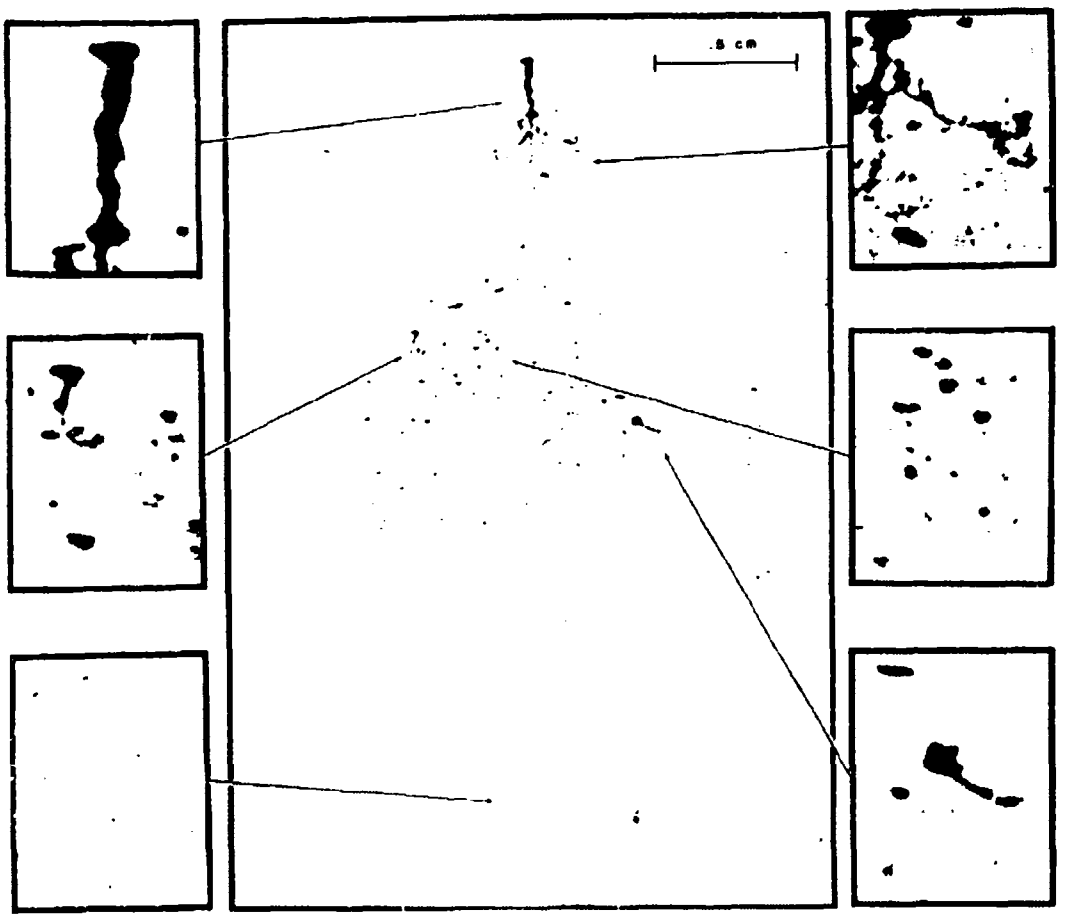

Figure 8. Primary Fragments Resulting from Metal Droplet Breakup (Series 11, Table II)

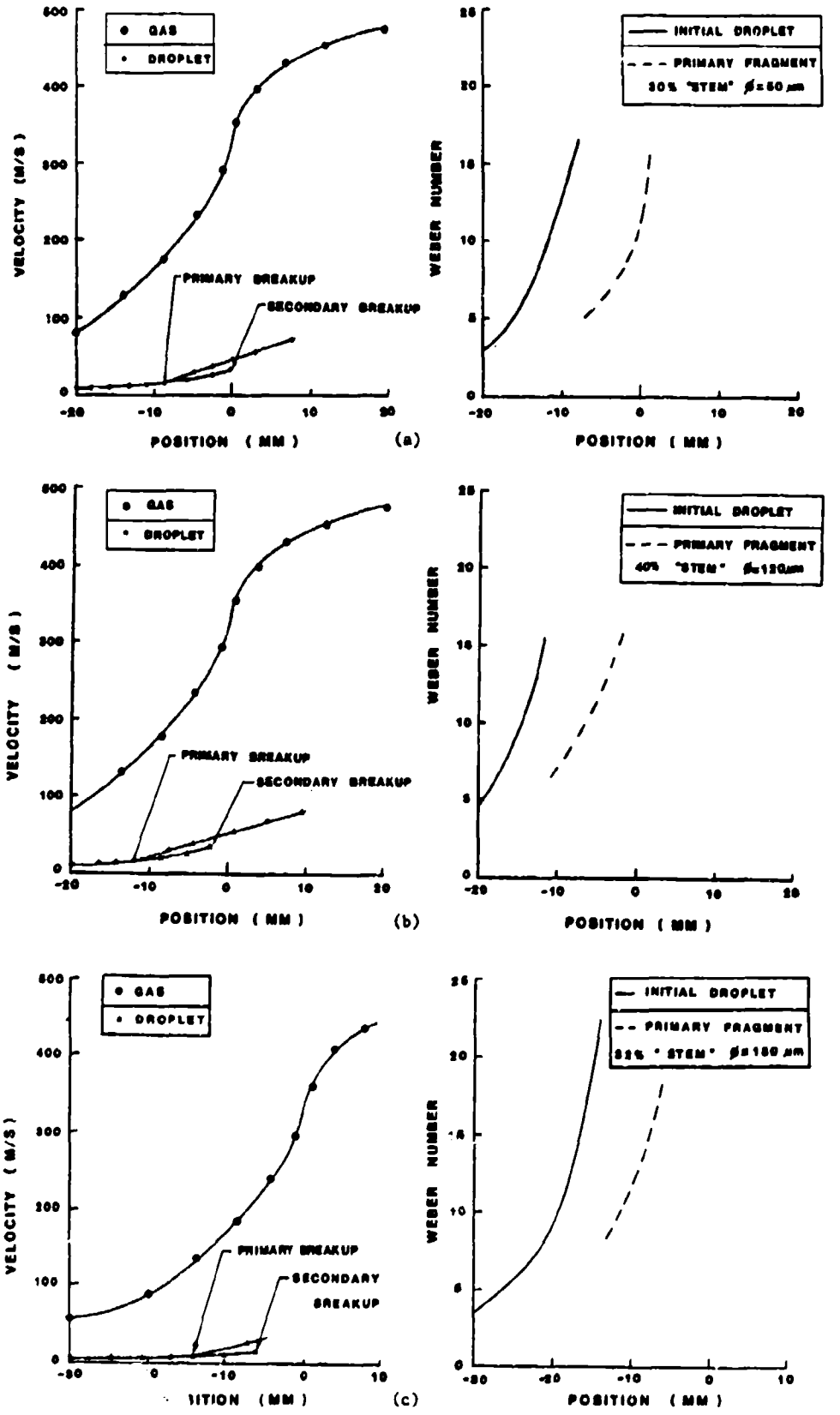

Figure 9. Metal Droplet Velocity and Weber Number Profiles:
(a) Series 9, (b) Series 10, and (c) Series 11 (Table II)

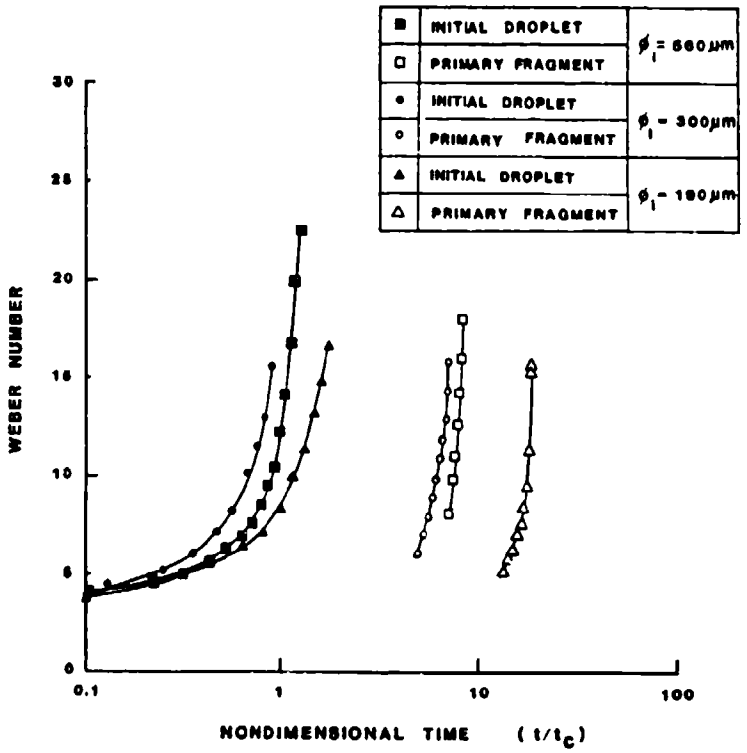

Figure 10. Metal Droplet Weber Number Histories

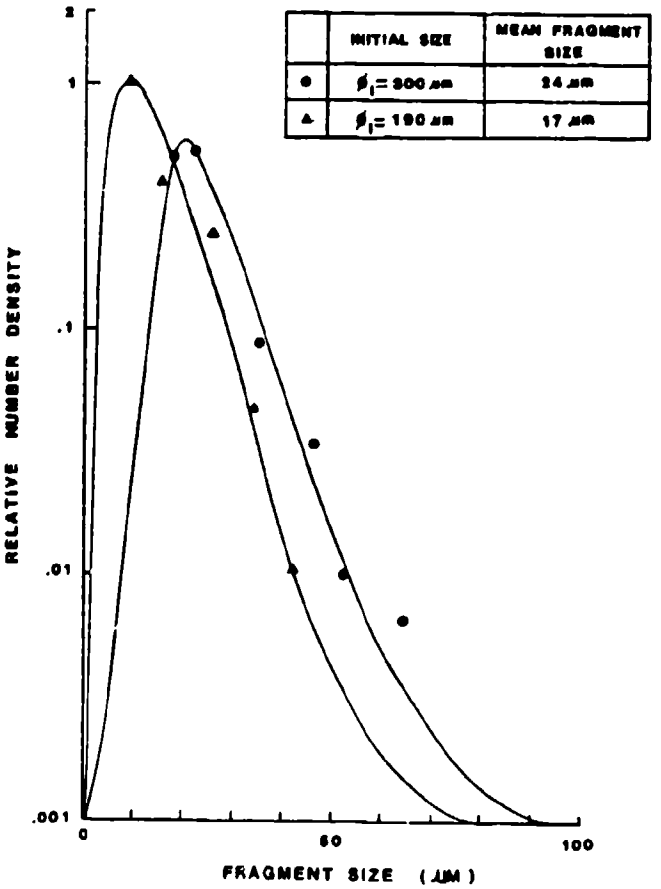

Figure 11. Fragment Number Density/Size Distribution